




# DISSOLUTION RATES OF ALLOPHANE WITH VARIABLE Fe CONTENTS: IMPLICATIONS FOR AQUEOUS ALTERATION AND THE PRESERVATION OF X-RAY AMORPHOUS MATERIALS ON MARS

S. J. RALSTON<sup>1,2,\*</sup> , ELISABETH M. HAUSRATH<sup>1</sup>, OLIVER TSCHAUNER<sup>1</sup>, ELIZABETH RAMPE<sup>3</sup>,  
TANYA S. PERETYAZHKO<sup>2</sup>, ROY CHRISTOFFERSEN<sup>2</sup>, CHRIS DEFELICE<sup>1</sup>, AND HYEJEONG LEE<sup>1</sup>

<sup>1</sup>University of Nevada, Las Vegas, 4505 S Maryland Pkwy, Las Vegas, NV 89154, USA

<sup>2</sup>Jacobs, NASA Johnson Space Center, Mail Code XI3, Houston, TX 77058, USA

<sup>3</sup>NASA Johnson Space Center, Houston, TX 77058, USA

**Abstract**—Recent measurements from Mars document X-ray amorphous/nano-crystalline materials in multiple locations across the planet. Despite their prevalence, however, little is known about these materials or what their presence implies for the history of Mars. The X-ray amorphous component of the martian soil in Gale crater has an X-ray diffraction pattern that can be fit partially with allophane (approximately  $\text{Al}_2\text{O}_3 \cdot (\text{SiO}_2)_{1.3-2} \cdot (\text{H}_2\text{O})_{2.5-3}$ ), and the low-temperature water-release data are consistent with allophane. The chemical data from Gale crater suggest that other silicate materials similar to allophane, such as Fe-substituted allophane (approximately  $(\text{Fe}_2\text{O}_3)_{0.01-0.5}(\text{Al}_2\text{O}_3)_{0.5-0.99} \cdot (\text{SiO}_2)_2 \cdot 3\text{H}_2\text{O}$ ), may also be present. In order to investigate the properties of these potential poorly crystalline components of the martian soil, Fe-free allophane (Fe:Al = 0), Fe-poor allophane (Fe:Al = 1:99), and Fe-rich allophane (Fe:Al = 1:1) were synthesized and then characterized using electron microscopy and Mars-relevant techniques, including infrared spectroscopy, X-ray diffraction, and evolved gas analysis. Dissolution experiments were performed under acidic (initial pH values  $\text{pH}_0 = 3.01$ ,  $\text{pH}_0 = 5.04$ ), near-neutral ( $\text{pH}_0 = 6.99$ ), and alkaline ( $\text{pH}_0 = 10.4$ ) conditions in order to determine dissolution kinetics and alteration phases for these poorly crystalline materials. Dissolution rates ( $r_{\text{diss}}$ ), based on the rate of Si release into solution, show that these poorly crystalline materials dissolve approximately an order of magnitude faster than crystalline phases with similar compositions at all pH conditions. For Fe-free allophane,  $\log r_{\text{diss}} = -10.65 - 0.15 \times \text{pH}$ ; for Fe-poor allophane,  $\log r_{\text{diss}} = -10.35 - 0.22 \times \text{pH}$ ; and for Fe-rich allophane,  $\log r_{\text{diss}} = -11.46 - 0.042 \times \text{pH}$  at 25°C, where  $r_{\text{diss}}$  has the units of  $\text{mol m}^{-2} \text{s}^{-1}$ . The formation of incipient phyllosilicate-like phases was detected in Fe-free and Fe-rich allophane reacted in aqueous solutions with  $\text{pH}_0 = 10.4$  (steady-state  $\text{pH} \approx 8$ ). Mars-analog instrument analyses demonstrate that Fe-free allophane, Fe-poor allophane, and Fe-rich allophane are appropriate analogs for silicate phases in the martian amorphous soil component. Therefore, similar materials on Mars must have had limited interaction with liquid water since their formation. Combined with chemical changes expected from weathering, such as phyllosilicate formation, the rapid alteration of these poorly crystalline materials may be a useful tool for evaluating the extent of aqueous alteration in returned samples of martian soils.

**Keywords**—Allophane · Amorphous phases · Kinetics · Mars · Mineral dissolution · Weathering · XRD

## INTRODUCTION

Recent observations have shown that Mars likely once had abundant liquid water (e.g. Carr 1996; Bibring et al. 2006; Vaniman et al. 2014; Grotzinger et al. 2015), widely considered to be a critical prerequisite for life. The amount of liquid water that was present on Mars, and how long it was present, is not yet clear, however. Clues to the characteristics and longevity of ancient aquatic environments on Mars may lie in aqueous alteration products, including the poorly crystalline, nano-crystalline, or X-ray amorphous

soil components (referred to here as ‘amorphous’ for simplicity) that have been detected widely on Mars from orbit (e.g. Singer 1985; Milliken et al. 2008; Rampe et al. 2012; Weitz et al. 2014) and in situ by the *Pathfinder*, *Spirit*, and *Curiosity* rovers (e.g. Morris et al. 2000; Squyres et al. 2008; Bish et al. 2013). Amorphous materials containing structural or adsorbed water may be the source of globally distributed hydrogen observed on Mars (Meslin et al. 2013). One such material, allophane (approximately  $\text{Al}_2\text{O}_3 \cdot (\text{SiO}_2)_{1.3-2} \cdot (\text{H}_2\text{O})_{2.5-3}$ ), has been detected from orbit across many regions of Mars (Rampe et al. 2011, 2012; Bishop and Rampe 2016), and has been proposed as a possible component of the amorphous material at Gale crater, the landing site of the Mars Science Laboratory rover, *Curiosity* (Bish et al. 2013; Dehouck et al. 2014).

\* E-mail address of corresponding author: silas.ralston@nasa.gov

DOI: 10.1007/s42860-021-00124-x

© The Clay Minerals Society 2021

Allophane is a poorly ordered aluminosilicate that forms on Earth from the weathering of volcanic rocks and ash in moist, temperate climates (e.g. Wada 1989; Parfitt 1990; Gustafsson et al. 1998). Allophane has short-range atomic order and forms aggregates of hollow, porous nano-scale spherules ~50 Å in diameter (Abidin et al. 2004), giving it a large adsorption capacity and a large surface area (Ohashi et al. 2002; Iyoda et al. 2012). Allophanes can have a range of Al:Si ratios, and at Al:Si ratios below ~2:1, the 'excess' Si is polymerized in the interior of the allophane nano-spherules (Childs et al. 1990; Parfitt 1990). In Fe-rich soils, Fe<sup>3+</sup> can substitute isomorphically for some or most of the Al, producing Fe-substituted allophane (e.g. Kitagawa 1973) or a related mineral, hisingerite (approximately Fe<sup>3+</sup><sub>2</sub>Si<sub>2</sub>O<sub>5</sub>(OH)<sub>4</sub>·H<sub>2</sub>O, Henmi et al. 1980). Like allophane, hisingerite is poorly ordered and tends to form aggregates of hollow, porous nano-spherules in soils (Ingles and Willoughby 1967), although the nano-spherules are much larger (~200 Å in diameter as per Shayan 1984).

Measurements from the Chemistry and Mineralogy (CheMin) instrument aboard *Curiosity* indicate that amorphous material is present in abundances from ~15–70 wt.% in all samples measured to date (e.g. Bish et al. 2013; Blake et al. 2013; Dehouck et al. 2014; Vaniman et al. 2014; Treiman et al. 2016; Rampe et al. 2017; Sutter et al. 2017). The broad hump in the CheMin X-ray diffraction (XRD) patterns of these samples, which was assigned to amorphous material, has been fit by a combination of allophane, ferrihydrite, and/or rhyolitic and basaltic glass for samples of modern aeolian sediment (e.g. the Rocknest aeolian bedform; Bish et al. 2013; Achilles et al. 2017) and ancient sandstone and mudstone (e.g. the Cumberland, John Klein, and Windjana drill sites; Vaniman et al. 2014; Treiman et al. 2016; Rampe et al. 2017). Plausible chemical composition of the amorphous component for inactive aeolian sediment (i.e. soil) was estimated by subtracting the calculated composition of the crystalline component (determined from CheMin data) from the bulk sample composition obtained from *Curiosity's* Alpha Particle X-Ray Spectrometer (APXS) (Bish et al. 2013; Dehouck et al. 2014; Vaniman et al. 2014). Based on the Fe-rich nature of the material, hisingerite may be present instead of or in addition to allophane (Bish et al. 2013; Dehouck et al. 2014).

Weathering of basaltic materials on Mars could have produced amorphous silica and Al-rich clay minerals if the water:rock ratio was high (e.g. Catalano 2013). Amorphous silica and Al-rich clay minerals on Mars may represent the final stages of an alteration sequence in which allophane is an intermediate product. Although much research has been done on the structure of allophane (e.g. Childs et al. 1990; Ohashi et al. 2002; Montarges-Pelletier et al. 2005; Iyoda et al. 2012; Bishop et al. 2013), few data exist on its alteration mechanisms, including dissolution kinetics (Abidin et al. 2004), and to the present authors' knowledge no dissolution rates have been measured for Fe-rich allophane.

The objectives of this study were, therefore, to determine the rates and conditions under which analogs for the

martian amorphous soil component persist, dissolve, and form secondary alteration phases. To those ends, the study intended to synthesize Fe-free allophane, Fe-poor allophane, and Fe-rich allophane, and to perform batch dissolution experiments of these phases in acidic, near-neutral, and alkaline conditions; and to characterize the altered materials. The desired outcome was that the results could then help to place constraints on the characteristics and longevity of liquid water that was present in allophane-bearing regions on Mars after the formation of these amorphous materials and help to search for direct evidence of past aqueous alteration in returned martian samples.

## MATERIALS AND METHODS

### *Synthesis Procedures*

Fe-free allophane, Fe-poor allophane, and Fe-rich allophane were synthesized following the methods of Baker and Strawn (2012, 2014) and Baker et al. (2014). Plastic labware was used for all steps of the synthesis in order to avoid silica contamination from glass.

Syntheses were carried out using AlCl<sub>3</sub>·6H<sub>2</sub>O (reagent grade, Alfa Aesar, Haverhill, Massachusetts, USA), FeCl<sub>3</sub>·6H<sub>2</sub>O (ACS grade, Mallinckrodt, Staines-upon-Thames, UK), and tetraethyl orthosilicate (TEOS) (≥98% purity, Acros Organics, Fair Lawn, New Jersey, USA). Solutions of 0.1 M AlCl<sub>3</sub> and FeCl<sub>3</sub> were mixed, and TEOS was added. While stirring, a solution of 1 M NaOH (reagent grade, VWR Chemicals BDH, Poole, UK) was added to the solution with a variable-speed Just Infusion syringe pump (Model NE-300, New Era Pump Systems Inc., East Farmingdale, New York, USA) at a rate of 25 mL h<sup>-1</sup> in order to hydrolyze TEOS and allow Si to bond with Al and Fe. The NaOH solution was added until a molar ratio of OH/(Al + Fe) = 3:1 was achieved in order to maximize allophane production and minimize the production of other phases, such as imogolite (Denaix 1993). The recipes used for synthesis of Fe-free allophane, Fe-poor allophane, and Fe-rich allophane, along with the Al:Fe:Si molar ratio, Brunauer-Emmett Teller (BET) specific surface area (SSA), and average particle size of each unaltered material, are summarized in Table 1. The precursor materials were stirred for one additional hour after NaOH addition to ensure thorough mixing, and then incubated without stirring at room temperature overnight to stabilize the suspension through an initial stage of colloid formation and proton release (Denaix 1993; Montarges-Pelletier et al. 2005). The precursors were then heated in an oven at 95°C for 7 days to promote colloid growth and maturation. The samples were removed from the oven, cooled on the lab bench to room temperature, and washed with 18.2 MΩ cm deionized water until the conductivity of the supernatant was <20 μS to remove excess ions and alcohol from TEOS. The washed products were frozen in a -20°C freezer for at least 24 h, and then

**Table 1** Synthesis recipes, Al:Fe:Si molar ratios, BET SSA, and particle sizes for Fe-free allophane, Fe-poor allophane, and Fe-rich allophane. NaOH was used to hydrolyze TEOS to allow Si to bind with Al and Fe

Material	0.1 M AlCl <sub>3</sub> (mL)	0.1 M FeCl <sub>3</sub> (mL)	TEOS (mL)	1 M NaOH (mL)	Al:Fe:Si molar ratio*	BET SSA (m <sup>2</sup> g <sup>-1</sup> )	Particle size (μm)
Fe-free allophane	167.00	0.00	3.72	50.00	1:0:1	385.77 ± 0.15	167.5 ± 2.2
Fe-poor allophane	165.33	1.67	3.72	50.00	0.99:0.01:1	350.24 ± 10.67	133.1 ± 0.8
Fe-rich allophane	83.5	83.5	3.72	50.00	0.5:0.5:1	507.48 ± 0.22	166.5 ± 4.9

\*Synthesis ratios. The compositions of the final solids measured via total digestion were slightly more Al-rich than the synthesis ratios (Table 6)

freeze-dried to create the final solid product. Samples were sieved to < 355 μm prior to use in dissolution experiments.

#### Characterization of Unaltered Material

The synthesized Fe-free allophane, Fe-poor allophane, and Fe-rich allophane were characterized by Fourier-transform infrared photoacoustic spectroscopy (FTIR-PAS), X-ray diffraction (XRD), evolved gas analysis (EGA), scanning electron microscopy/energy dispersive X-ray spectroscopy (SEM/EDS), field-emission SEM (FE-SEM), field-emission scanning transmission electron microscopy (FE-STEM), BET SSA analysis, particle-size analysis, and total chemistry by total digestion.

**FTIR-PAS.** FTIR-PAS analyses were carried out on a Varian FTS 7000 FTIR spectrometer with a photoacoustic detector (Varian Inc., Palo Alto, California, USA) in the Inorganic Materials & Nanomaterials lab at the University of Nevada, Las Vegas, USA (UNLV). The use of photoacoustic techniques allowed samples to be analyzed with minimal preparation and was non-destructive to the sample. Absorption spectra were obtained on loosely packed powdered samples. For all runs, the scanning speed was 2.5 kHz, with 64 scans collected at a resolution of 4 cm<sup>-1</sup> over the range 4000–400 cm<sup>-1</sup> (2.5–25 μm). For each sample, the sample chamber with the sample was run through an open helium purge for 10 min, followed by a closed helium purge for another 10 min in order to minimize contamination from atmospheric gases. Carbon black was used to obtain a background spectrum for each run, and this background spectrum was used as a correction for all sample spectra in order to remove absorptions due to CO<sub>2</sub> and other atmospheric gases.

**XRD.** XRD patterns for unreacted Fe-free allophane, Fe-poor allophane, and Fe-rich allophane were obtained using a PANalytical X'Pert Pro MPD 3040 instrument (Malvern Panalytical Ltd., Malvern, UK) with a traditional spinner stage at NASA Johnson Space Center.

CoKα radiation was used for all samples for comparison to CheMin XRD data. The scans were conducted at 45 kV/40 mA, from 2 to 80°2θ with a step size of 0.02°2θ, 100 s per step. Before analysis, samples were crushed gently in an agate mortar and pestle to break up aggregates and sieved to < 75 μm. Silicon zero-background slides in aluminum sample holders were used for all samples.

**EGA.** Evolved gas analysis was conducted on Fe-free allophane, Fe-poor allophane, and Fe-rich allophane in order to compare these synthetic materials with those measured in Gale crater by the Sample Analysis at Mars (SAM) instrument on the *Curiosity* rover. EGA was conducted under conditions similar to those utilized by SAM (i.e. ramp rate, pressure, and carrier gas). The analyses were conducted in a Setaram LabSys Evo thermal gravimeter/differential scanning calorimeter (TG/DSC) furnace (Setaram Inc., Caluire, France) coupled to a Pfeiffer ThermoStar GSD 320 quadrupole mass spectrometer (Pfeiffer Vacuum, Aßlar, Germany) at NASA Johnson Space Center. The temperature range was from 30 to 1000°C with a ramp rate of 35°C min<sup>-1</sup>. The carrier gas was helium, with a flow rate of 10 mL min<sup>-1</sup>, and the pressure was 30 mbar. Approximately 10 mg of sample was used for each run, and samples were run in duplicate.

**Microscopy.** Freeze-dried aggregates of unaltered Fe-free allophane, Fe-poor allophane, and Fe-rich allophane were placed on carbon tape atop aluminum sample plugs and carbon coated for analysis using a Denton Vacuum DV-502A carbon coater (Denton Vacuum LLC, Moorestown, New Jersey, USA). SEM and EDS analyses were carried out on a JEOL scanning electron microscope model JSM-5600 (JEOL Ltd., Akishima, Tokyo, Japan) with a magnification range of 35× to 100,000× (1 μm resolution) with an Oxford ISIS EDS system (Oxford Instruments, Abingdon, UK) in the Electron Microanalysis and Imaging Laboratory (EMiL) at UNLV.

In order to reach sufficient magnifications to distinguish the nano-spherules characteristic of allophane, samples were examined using a JEOL JSM-6700F field-emission SEM (JEOL Ltd., Akishima, Tokyo, Japan) with a magnification range of 500 to  $430,000\times$  ( $5\ \mu\text{m}$ – $10\ \text{nm}$  resolution) in the EMiL at UNLV. Sample preparation was the same as for SEM/EDS analyses. A standard voltage of 15 kV was used, with a working distance of  $8.4\pm 0.1\ \text{mm}$ . Fe-free allophane was examined in secondary electron mode to investigate topography of particles, whereas Fe-poor and Fe-rich allophane were examined in backscatter mode to investigate potential chemical variations within and between particles.

Transmission electron microscopy was carried out using a JEOL JEM-2500SE analytical field-emission scanning transmission electron microscope (FE-STEM) (JEOL Ltd., Akishima, Tokyo, Japan) with up to  $1,000,000\times$  magnification ( $1.5\ \text{nm}$  resolution) at NASA Johnson Space Center. Both conventional and STEM bright-field imaging were used in order to identify major morphological features of the grains, such as nano-spherules. Assessment of features on the crystal-structure scale, including those indicative of short- or long-range atomic order, was achieved using high-resolution lattice fringe imaging (HRTEM). Freeze-dried samples were crushed gently in an agate mortar and pestle to break up aggregates, suspended in ethanol, and droplet-deposited on amorphous holey-carbon films supported on 200 mesh transmission electron microscope (TEM) grids (Electron Microscopy Sciences, Hatfield, Pennsylvania, USA). The major-element composition of grains was assessed by EDS.

*BET surface area and particle-size analysis.* Approximately 400 mg each of unreacted, unground synthetic Fe-free allophane, Fe-poor allophane, and Fe-rich allophane, sieved to the  $<355\ \mu\text{m}$  size fraction used in the dissolution experiments, were prepared for determination of BET SSA and particle-size analysis. The BET SSA values were used to normalize the calculated dissolution rates to surface area and allow comparison of calculated rates to the literature. BET SSA was determined using a Micromeritics TriStar II 3020 surface area and porosity instrument (Micromeritics Instrument Corporation, Norcross, Georgia, USA) at NASA Johnson Space Center.  $\text{N}_2$  was used as the analysis adsorbate. Samples were degassed at  $250^\circ\text{C}$  under vacuum overnight to remove adsorbed water, which can interfere with accurate BET results by occupying adsorption sites and preventing the analysis adsorbate from adsorbing. This temperature was chosen because it exceeds the temperature of water release for allophane ( $100$ – $150^\circ\text{C}$ , Bish and Duffy 1990; Rampe et al. 2016) but is well below the temperature at which allophane begins to transform to mulite ( $900$ – $950^\circ\text{C}$ , Parfitt 1990). Particle-size analysis was conducted on a Microtrac Bluewave S4640 particle size analyzer (MicrotracBEL, Osaka, Japan) at NASA Johnson Space Center. Samples were dispersed in ethanol and sonicated prior to analysis. All analyses were run in duplicate to allow estimates of uncertainty.

*Total chemistry.* Digestions were performed following a modification of the method of Potts et al. (1984) in order to quantify changes in chemical composition due to alteration. For each sample,  $\sim 0.1\ \text{g}$  of material was mixed in a 1:5 mass ratio with lithium tetraborate ( $\geq 98\%$ , Acros Organics, Fair Lawn, New Jersey, USA). The dry mixture was heated at  $975^\circ\text{C}$  in a graphite crucible for 20 min, and then allowed to cool to room temperature. The melt bead was removed from the crucible, mixed with 100 mL of 1 M  $\text{HNO}_3$  (Mallinkrodt, Staines-upon-Thames, UK) and stirred for 1 h on low heat ( $\sim 40^\circ\text{C}$ ). Another 100 mL of 1 M  $\text{HNO}_3$  was added after 1 h, and the suspension was stirred for an additional 1 h on low heat until the melt bead dissolved fully. The solution was stirred at room temperature overnight to ensure complete dissolution of silica species. After the overnight stirring step, an aliquot of the solution was filtered to  $0.2\ \mu\text{m}$  and sent to UNLV for Al-Si-Fe measurements using an iCAP Qc Inductively Coupled Plasma Mass Spectrometer (ICP-MS) (Thermo Scientific, Waltham, Massachusetts, USA). Graphite residues were observed on the filters due to graphite coatings on the original melt beads, but no other residues (i.e. incompletely dissolved sample) were observed on the filters. Filtered sample solutions were diluted by a factor of 100 for Si and Fe measurements, and by a factor of 1000 for Al measurements. Synthetic multi-element standard solutions were made from HPS™ single-element standard solutions (High Purity Standards, North Charleston, South Carolina, USA) and were used to construct standard calibration curves. The peaks of  $^{27}\text{Al}$ ,  $^{28}\text{Si}$ ,  $^{29}\text{Si}$ , and  $^{57}\text{Fe}$  were monitored under kinetic energy discrimination (KED) mode with collision cell gas to remove molecular interferences. The blank correction was typically  $<15\%$  for Si,  $<6\%$  for Fe, and  $<1\%$  for Al. The sensitivity drift within each analytical sequence was  $<15\%$ , and it was corrected by using an external drift monitor (e.g. DeFelice et al. 2019). Each solution was measured twice in two analytical sequences. These two measurements agreed within  $\pm 3\%$ , and their averages were reported.

#### *Dissolution Experiments and Solution Chemistry Analysis*

Experiments were prepared by adding  $150.0\pm 0.4\ \text{mg}$  of sample (Fe-free allophane, Fe-poor allophane, or Fe-rich allophane, sieved to  $<355\ \mu\text{m}$ ) to acid-washed 250 mL polypropylene bottles containing 180 mL of 0.01 M NaCl solution (made with reagent-grade NaCl, VWR Chemicals BDH, Poole, UK) adjusted to pH 3, 5, 7, or 10.4. The bottles were shaken in a shaker water bath at  $25.0\pm 0.1^\circ\text{C}$  at 50 rpm. The pH was adjusted with high-purity concentrated  $\text{HNO}_3$  or NaOH. Experiments were performed in batch to examine changes in the solid material under steady-state conditions, such as formation of incipient phyllosilicates, probably relevant to low water:rock (W/R) ratio isochemical reactions that may have occurred on Mars. The pH was not buffered due to the potential for changes in reaction rate and mechanism caused by the presence of buffers in solution (e.g. Dove and Crerar 1990; Wogelius and Walther 1991; Stillings and Brantley 1995). However,

0.01 M NaCl solution was used instead of deionized water to reduce drastic changes in ionic strength due to dissolution, which can significantly affect the dissolution rates of high-silica materials compared to dissolution in pure water (Dove and Nix 1997; Icenhower and Dove 2000). Each experiment was run in duplicate with one blank under each pH condition. Blanks consisted of 0.01 M NaCl solution with no added allophane, with the same amount of HNO<sub>3</sub> or NaOH added as in the experiments. Solution aliquots (10 mL each) were taken periodically based on expected dissolution rates of similar materials (e.g. Liang and Readey 1987; Icenhower and Dove 2000; Huertas et al. 2001; Gislason and Oelkers 2003; Abidin et al. 2004; Rozalen et al. 2008; Gainey et al. 2014; Steiner et al. 2016) and preliminary experiments. The resulting change in water:sample ratio was corrected when calculating the elemental release rate (see the Calculations section below). The first 8 mL of each sample aliquot was filtered through a 0.2 µm filter and acidified with 1% v/v high purity HNO<sub>3</sub> (67–70%, VWR Chemicals BDH, Poole, UK). The pH of the solution was measured from the remaining 2 mL of unfiltered sample aliquot. Dissolution experiments are summarized in Table 2, and the full experimental conditions for each experiment, including initial and final pH and total reaction time, are given in the Supplementary Material (Data Sheets S1–S38). Experiments are referred to by the starting pH (pH<sub>0</sub>) and material: Fe-free allophane (FFA), Fe-poor allophane (FPA), or Fe-rich allophane (FRA). For example, a dissolution experiment with Fe-free allophane and an initial pH of 3 would be referred to as ‘pH<sub>0</sub>\_3\_FFA’.

Elemental analyses for dissolved Fe, Al, and Si were conducted via flame atomic absorption (AA) spectroscopy on a Thermo Scientific iCE 3000 Series AA Spectrometer

(Thermo Scientific, Waltham, Massachusetts, USA) at UNLV. Dissolved Fe was measured using an air-acetylene flame and had a practical quantitation limit of 0.2 mg L<sup>-1</sup>. The practical quantitation limit is defined as the concentration at which the instrument response is roughly 10 times greater than the standard deviation of the calibration (Gibbons et al. 1991). Dissolved Al and Si were measured using an air-acetylene-nitrous oxide flame and had practical quantitation limits of 1.0 mg L<sup>-1</sup> and 0.2 mg L<sup>-1</sup>, respectively. Fe samples were treated with CaCO<sub>3</sub> (ACS grade, RICCA Chemical Company, Arlington, Texas, USA) to reduce interference, and Al samples were treated with KCl (molecular biology grade, EMD Millipore, Burlington, Massachusetts, USA) to control ionization, following the methods of Eaton et al. (2005), and 18.2 MΩ cm deionized water was used as an instrument blank.

### Calculations

Dissolution rates were determined from moles of Si released into solution with time. The Si concentration measured in solution was corrected for volume removed during sampling to obtain moles of Si released using the equation:

$$m_t = m_{(t-1)} + (c_t - c_{(t-1)})V_{(t-1)} \quad (1)$$

where  $m_t$  and  $m_{(t-1)}$  are the moles of Si released at times  $t$  and  $t-1$ ,  $c_t$  and  $c_{(t-1)}$  are the corresponding concentrations (mol L<sup>-1</sup>), and  $V_{(t-1)}$  is the volume of solution (L) remaining at time  $t-1$  (Welch and Ulmann 2000). Dissolution of all materials showed an initial linear rapid Si release phase, followed by a slower phase that approached steady conditions (Fig. 1). This approach to steady conditions was expected in batch (closed-system) conditions either due to

**Table 2** Table of dissolution experiments

Experiment name	Material	Starting solution	Initial pH (pH <sub>0</sub> )	Starting mass (mg)
pH <sub>0</sub> _3_FFA	Fe-free allophane	0.01 M NaCl+HNO <sub>3</sub>	3.01	150.00 ± 0.10
pH <sub>0</sub> _3_FPA	Fe-poor allophane	0.01 M NaCl+HNO <sub>3</sub>	3.01	150.25 ± 0.05
pH <sub>0</sub> _3_FRA	Fe-rich allophane	0.01 M NaCl+HNO <sub>3</sub>	3.01	149.95 ± 0.35
pH <sub>0</sub> _3_BLANK	NA	0.01 M NaCl+HNO <sub>3</sub>	3.01	0
pH <sub>0</sub> _5_FFA	Fe-free allophane	0.01 M NaCl+HNO <sub>3</sub>	5.04	149.85 ± 0.25
pH <sub>0</sub> _5_FPA	Fe-poor allophane	0.01 M NaCl+HNO <sub>3</sub>	5.04	149.85 ± 0.05
pH <sub>0</sub> _5_FRA	Fe-rich allophane	0.01 M NaCl+HNO <sub>3</sub>	5.04	149.85 ± 0.25
pH <sub>0</sub> _5_BLANK	NA	0.01 M NaCl+HNO <sub>3</sub>	5.04	0
pH <sub>0</sub> _7_FFA	Fe-free allophane	0.01 M NaCl+NaOH	6.99	150.10 ± 0.10
pH <sub>0</sub> _7_FPA	Fe-poor allophane	0.01 M NaCl+NaOH	6.99	150.2*
pH <sub>0</sub> _7_FRA	Fe-rich allophane	0.01 M NaCl+NaOH	6.99	149.80 ± 0.10
pH <sub>0</sub> _7_BLANK	NA	0.01 M NaCl+NaOH	6.99	0
pH <sub>0</sub> _10_FFA	Fe-free allophane	0.01 M NaCl+NaOH	10.36	150.30 ± 0.10
pH <sub>0</sub> _10_FPA	Fe-poor allophane	0.01 M NaCl+NaOH	10.36	149.95 ± 0.35
pH <sub>0</sub> _10_FRA	Fe-rich allophane	0.01 M NaCl+NaOH	10.36	150.00 ± 0.30
pH <sub>0</sub> _10_BLANK	NA	0.01 M NaCl+NaOH	10.36	0

NA: none added

\*Duplicate experiment excluded because of low mass (73.7 mg), high standard error, and poor R<sup>2</sup> value (Data Sheet S18)

equal rates of silica dissolution from one phase and silica precipitation to another phase, or due to true chemical equilibrium with respect to some silica-containing phase. The initial linear part of the curve was determined by fitting a preliminary regression line through the Si release data for the first 7 h of the experiment (generally equivalent to the first 3–4 points), and the last data point that was within two standard deviations ( $2\sigma$ ) of this line was considered the final point of the linear part of the curve. This approach is similar to the method used by Abidin et al. (2004) to determine the point at which allophane dissolution transitions from an initial, rapid rate to a slower rate approaching steady-state. The section of the Si-release curve between zero and the first time point was not included in these calculations, as it may represent release of Si due to rapid dissolution of fine particles (e.g. Nagy et al. 1991), and would therefore not be representative of the dissolution rate of the bulk material. When the first point had a greater silica concentration than the second point (both replicates of pH<sub>0</sub>\_5\_FRA, one replicate each of pH<sub>0</sub>\_5\_FFA and pH<sub>0</sub>\_5\_FPA), the first point was not included in the regression, as this was interpreted as inadvertent sampling of solid material. The initial linear part of the Si-release curve, determined as described above, was then fit with a linear regression, where the slope of the line was the silica release rate in mol s<sup>-1</sup>. The dissolution rate was calculated using the following equation:

$$r_{\text{diss}} = \frac{\Delta m / \Delta t}{A \times M} \quad (2)$$

where  $r_{\text{diss}}$  is the dissolution rate (mol m<sup>-2</sup> s<sup>-1</sup>),  $\Delta m / \Delta t$  is the silica-release rate (mol s<sup>-1</sup>),  $A$  is the average initial BET SSA of the material (m<sup>2</sup> g<sup>-1</sup>), and  $M$  is the total mass of material in the reactor (g) (Table 3). One of the duplicate experiments of pH<sub>0</sub>\_7\_FPA was excluded from the rate calculations due to anomalous experimental conditions (see Data Sheet S18, Supplementary Material). Although BET surface area is not a perfect measurement of reactive surface area (e.g. Velbel 1993; Gautier et al. 2001; Sanders et al. 2012), it allows comparisons of these surface area-normalized dissolution rates to surface area-normalized measurements in the literature. The average pH of the linear section of the dissolution curve was considered to be the pH of the experiment, as the dissolution rate is also determined over the same section (see *Solution Chemistry* and Section S10, Supplementary Material).

Rate laws were determined by plotting the log of the dissolution rates from Eq. 2 against the pH of the experiment, and then fitting the points with a linear regression. The resulting rate law was of the form:

$$\log r_{\text{diss}} = \log k_{\text{diss}} - n \times \text{pH} \quad (3)$$

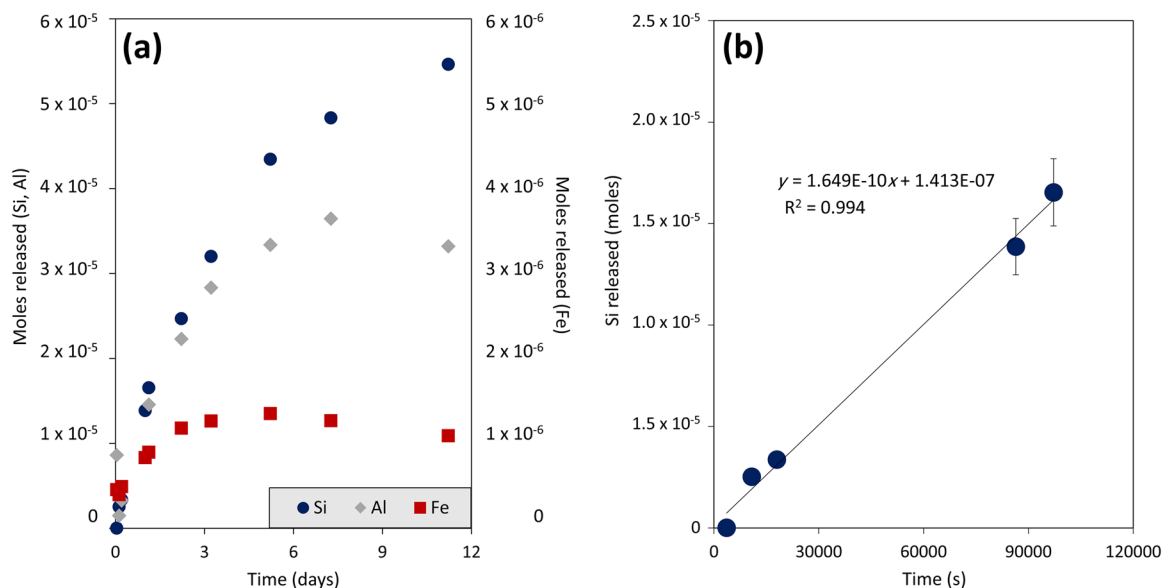


**Fig. 1** Representative solution-chemistry data for a dissolution experiment. **a** Typical shape of the Si, Al, and Fe release curves for Fe-free allophane, Fe-poor allophane, and Fe-rich allophane dissolution (note the difference in scale between Si and Al released versus Fe released). **b** The linear portion of the silica release curve as exemplified by a pH<sub>0</sub>\_3\_FRA experiment. The linear portion of the silica release curve was fit with a linear regression (equation and R<sup>2</sup> value shown). Error bars are the standard error of the AA measurement, and are smaller than the points for the first three points. In general, Fe-rich allophane reached higher final Si, Al, and Fe concentrations than Fe-free allophane or Fe-poor allophane (Figs S9–S14). No Al or Fe release was observed in experiments at pH<sub>0</sub> 5, 7, or 10. Fe release was only observed in Fe-rich allophane experiments at pH<sub>0</sub> 3. All data for all experiments are given in the Supplementary Material (Data Sheets S1–S38)

**Table 3** pH at the first time point ( $t_i$ ) and at the final time point ( $t_f$ ) of the data used to calculate the dissolution rates, the dissolution rates ( $r_{\text{diss}}$ ), and their  $1\sigma$  standard deviations (Std err). The '-1' or '-2' suffix indicates duplicate experiments. Averages of the data are plotted in Fig. 7 with rate laws calculated as described in the text. Cells in italics were omitted from the rate-law calculation due to anomalous experimental conditions (see Supplementary Material Data Sheet S18). All solution compositions for each experiment at each time point are given in Supplementary Material (Data Sheets S1–S38)

Material	pH 3			pH 5			pH 7			pH 10		
	pH at $t_i$	pH at $t_f$	Std err <sup>a</sup> $\times 10^{-12}$	pH at $t_i$	pH at $t_f$	Std err <sup>a</sup> $\times 10^{-12}$	pH at $t_i$	pH at $t_f$	Std err <sup>a</sup> $\times 10^{-12}$	pH at $t_i$	pH at $t_f$	Std err <sup>a</sup> $\times 10^{-12}$
Fe-free allophane-1	3.25	3.48	13.0	5.84	6.47	2.17	6.76	7.17	2.11	9.94	8.70	1.35
Fe-free allophane-2	3.22	4.09	5.57	5.77	6.39	2.05	6.65	7.06	2.28	9.90	8.46	1.30
Fe-poor allophane-1	3.21	4.04	5.70	5.59	5.98	1.95	6.38	6.40	1.39	9.81	7.80	1.09
Fe-poor allophane-2	3.24	3.48	14.7	5.55	6.05	1.88	6.37	6.35	1.49	9.78	7.39	0.716
Fe-rich allophane-1	3.07	3.23	2.17	5.63	6.56	2.41	5.94	5.27	2.29	10.04	7.08	1.45
Fe-rich allophane-2	3.07	3.54	2.48	5.50	6.46	1.85	6.05	5.24	2.31	10.03	6.85	1.50

<sup>a</sup> $r_{\text{diss}}$  and standard error have units of  $\text{mol m}^{-2} \text{s}^{-1}$

where  $k_{\text{diss}}$  is the dissolution rate constant, and  $n$  is the reaction order with respect to  $\text{H}^+$ .

In order to provide a comparison to studies of other rapidly dissolving phases (e.g. Elwood-Madden et al. 2012; Miller et al. 2016), particle lifetimes of Fe-free allophane, Fe-poor allophane, and Fe-rich allophane were calculated by the shrinking sphere model (Lasaga 1984):

$$t = \frac{d}{2r_{\text{diss}}V_m} \quad (4)$$

where  $t$  is the particle lifetime (s),  $d$  is the particle diameter (m),  $r_{\text{diss}}$  is the dissolution rate ( $\text{mol m}^{-2} \text{s}^{-1}$ ) from Eq. 3, and  $V_m$  is the molar volume ( $\text{m}^3 \text{mol}^{-1}$ ). The molar volume of all allophane samples was assumed to be  $\sim 101 \text{ cm}^3 \text{mol}^{-1}$  based on density values from Wada (1989) and calculated molecular mass because significant volume change is not expected due to Fe-substitution in allophanes (Baker et al. 2014). The particle lifetime was calculated for a particle 1  $\mu\text{m}$  in diameter to facilitate comparison with similar studies (e.g. Elwood-Madden et al. 2012; Miller et al. 2016), and for the measured particle sizes of allophane aggregates in the present study (given in Table 1). This calculation is presented as a first-order estimate of allophane particle lifetimes because allophane does not typically form solid, spherical particles in nature.

#### Characterization of Reacted Materials

Following dissolution experiments, the solution was decanted from the dissolution vessels and the solid material was centrifuged at  $15,557 \times g$  for 5 min, washed twice with deionized water to remove excess NaCl, and then frozen for at least 24 h before freeze-drying for analysis by SEM, FE-STEM, XRD, and total digestion. The same sample-preparation techniques and the same analytical conditions were used for altered material as for the unreacted material. A summary of characterizations is given in Table 4.

## RESULTS

#### Characterization of Unreacted Materials

**FTIR-PAS.** Infrared absorbance spectra for Fe-free allophane, Fe-poor allophane, and Fe-rich allophane (Fig. 2a) were similar to each other and consistent with previously published results (e.g. Wada, 1989; Montarges-Pelletier et al. 2005; Rampe et al. 2012; Bishop et al. 2013; Milliken and Bish 2014). All samples had absorption bands at 3400, 1645, 1030, and 940  $\text{cm}^{-1}$ , and a weak band near 620  $\text{cm}^{-1}$ , and varied from the literature values by  $< 50 \text{ cm}^{-1}$  (Supplementary Material, Fig. S1). A full description of absorption bands and their assignments is presented in the Supplementary Material.

**XRD.** Unreacted Fe-free allophane, Fe-poor allophane, and Fe-rich allophane had similar diffraction patterns with elevated low-angle background and broad peaks (Fig. 2b,

**Table 4** Summary of characterizations of altered synthetic materials

Method	Fe-free allophane			Fe-poor allophane			Fe-rich allophane		
	pH <sub>0</sub>	pH <sub>final</sub>	Duration (days)	pH <sub>0</sub>	pH <sub>final</sub>	Duration (days)	pH <sub>0</sub>	pH <sub>final</sub>	Duration (days)
SEM	NA	NA	NA	NA	NA	NA	3.02	5.35	2
							3.02	6.54	31
FE-STEM	10.36	8.59	57	NA	NA	NA	3.01	4.78	181
							10.36	6.39	57
XRD	3.01	4.42	20	3.01	4.35	20	3.01	3.97	20
	5.04	6.85	12	5.04	6.37	12	5.04	7.06	12
	6.99	7.20	93	6.99	6.40	93	6.99	5.00	93
	10.36	7.79	18	10.36	7.18	12	10.36	6.56	12
Total digestion	3.01	4.42	20	3.01	4.35	20	3.01	3.97	20
	5.04	6.85	12	5.04	6.37	12	5.04	7.06	12
	6.99	7.20	93	6.99	6.40	93	6.99	5.00	93
	10.36	7.79	18	10.36	7.18	18	10.36	6.56	18

NA = No analysis performed. The various durations for experiments with different pH<sub>0</sub> values allowed all experiments to reach steady-state regardless of dissolution rate

Fig. S2), indicating an abundance of small particles and nano-crystalline structure, respectively (van der Gaast and Vaars 1981). These synthetic materials have XRD patterns consistent with previous measurements of allophane and Fe-substituted allophane. The peak positions obtained by

XRD for unreacted, synthesized, Fe-free allophane, Fe-poor allophane, and Fe-rich allophane are presented in Table 5 along with literature values for natural and synthetic allophane samples and natural hisingerite samples. Mustoe (1996) presented a similar summary of the *d* spacings of

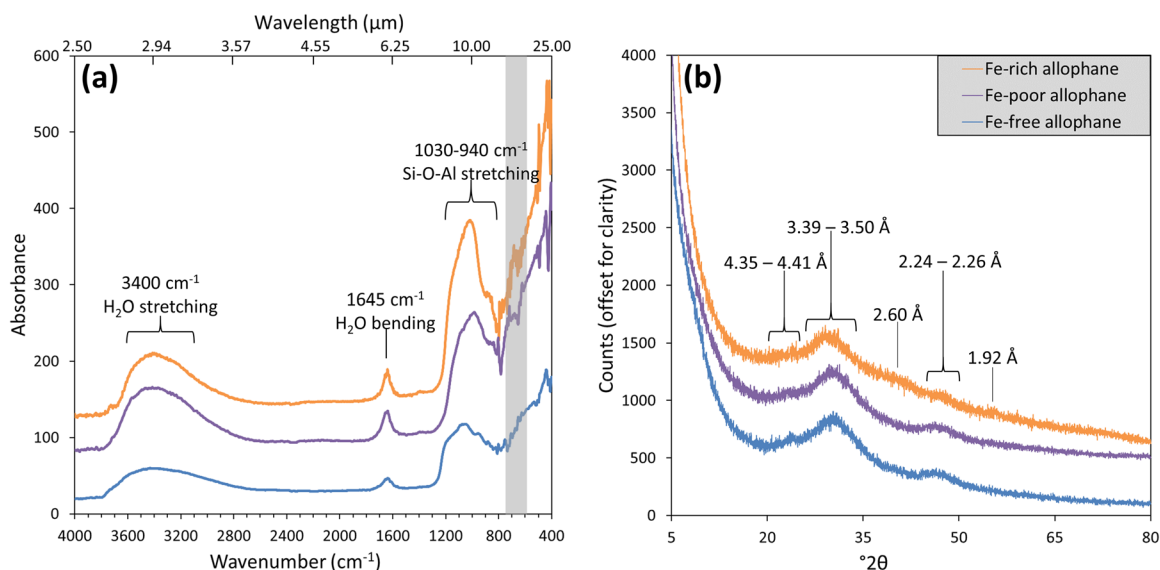


**Fig. 2** **a** FTIR-PAS absorption spectra of synthetic Fe-free allophane, Fe-poor allophane, and Fe-rich allophane. All samples had absorption bands at 3400, 1645, 1030, and 940 cm<sup>-1</sup> (labeled), and a weak band near 620 cm<sup>-1</sup> (shaded rectangular area), in agreement with literature values for allophane and hisingerite. The spectra are offset for clarity. **b** XRD patterns of unreacted synthetic Fe-rich allophane, Fe-poor allophane, and Fe-free allophane. In the Fe-rich allophane sample, a broad peak, indicative of nano-crystalline structure, is visible at ~3.50 Å (29.6°2θ), with minor broad peaks at 2.60, 2.24, and 1.92 Å (40.2, 47.1, and 55.5°2θ, respectively). In the Fe-poor allophane sample, broad peaks occur at 4.41, 3.42, and 2.26 Å (23.4, 30.3, and 46.6°2θ). In the Fe-free allophane sample, broad peaks occur at 4.35, 3.39, and 2.25 Å (23.7, 30.6, and 46.8°2θ). All samples show elevated background at low angle indicative of small particle sizes. CoKα radiation was used for all patterns



various natural hisingerite samples from many locations, indicating variations in  $d$  spacings of up to 0.3 Å, as well as variability in the number of observed peaks. Values for hisingerite are included as a proxy for Fe-rich allophane, as little literature exists on Fe-rich allophane (Ossaka et al. 1971; Farmer 1997; Baker and Strawn 2014).

**EGA.** Fe-free allophane, Fe-poor allophane, and Fe-rich allophane exhibited a sharp H<sub>2</sub>O release centered at ~130°C, probably due to release of adsorbed H<sub>2</sub>O (Fig. S3), followed by a broader release from ~130–400 °C which may be due to release of structural H<sub>2</sub>O, consistent with previous laboratory measurements of water release from allophane (e.g. Bish and Duffy 1990). Release of O<sub>2</sub> occurred concurrently with H<sub>2</sub>O release in all samples (Figs S3–S4), indicating that the O<sub>2</sub> production resulted from fragmentation of H<sub>2</sub>O during ionization in the mass spectrometer. Overall, these observations are consistent with previous EGA measurements for allophane (e.g. Bish and Duffy 1990; Rampe et al. 2016). Differential scanning calorimetry (DSC) performed concurrently with EGA agreed well with differential thermal analysis (DTA) of Fe-substituted allophanes by Ossaka et al. (1971), with a peak at 960 ± 10°C for Fe-free allophane that broadened and shifted to lower temperature with increasing Fe content (924 ± 1°C for Fe-poor allophane and 791 ± 1°C for Fe-rich allophane; Fig. S5).

**Microscopy.** In general, unreacted samples examined by SEM consisted of large, smooth grains ~300–600 µm across coated with much smaller (~10–50 µm) flakes of ‘fluffy’ material (Figs 3a and S6). Semi-quantitative EDS analyses, conducted concurrently with SEM investigations, yielded mainly Al, Si, and Fe compositions consistent with synthesis ratios, and no major compositional differences were observed between the larger, smooth grains and the smaller, ‘fluffy’ material (Table S1). FE-SEM analyses of unreacted material also showed that all samples contained small, ‘fluffy’ aggregates (e.g. Figs 3b and S7) as well as large chunks of material that are probably aggregates formed during centrifugation due to the rapid rotation speed (15,557 ×  $g$ ) required to pull fine particles out of suspension. Chloride was detected in a few samples, probably the result of incomplete washing, but was not prevalent (Table S1).

Particles with nano-spherule structures, indicative of allophane, were observed in the FE-STEM subsamples of the unreacted synthetic materials (Fig. 4). Nano-spherules have previously been observed in samples of natural allophane (e.g. Wada 1989; Iyoda et al. 2012) and natural hisingerite (e.g. Eggleton and Tilley 1998). The majority of Fe-rich allophane material was structurally disordered (i.e. amorphous) based on HRTEM images analyzed by Fourier-transform image processing (Fig. 4b). Some synthetic Fe-rich allophane particles exhibited poorly developed lattice fringes in localized regions (e.g. Fig. 4c), indicative of

**Table 5** A summary of the peak positions observed in various natural and synthetic allophane and hisingerite samples

Sample	Peak positions (Å)						
Allophane			3.3		2.25		
Al-rich allophane	12	4.3	3.4		2.2	1.9	1.7
Synthetic allophane			3.5		2.2		1.4
Unreacted synthetic Fe-free allophane (this study)	12.27	4.35	3.39		2.25		
Iron-coprecipitated allophane			3.56				
Unreacted synthetic Fe-poor allophane (this study)		4.41	3.42		2.26		
Hisingerite		4.4	3.5	2.5–2.6			1.4–1.5
Hisingerite from Geelong, Victoria, Australia		4.49		2.58			
Hisingerite from Riddarhyttan, Sweden	7.70	4.44	3.57	2.56	2.26	1.69	1.54
Hisingerite from Gillinge, Sweden	7.51	4.41	3.58	2.57	2.41	1.68	1.54
Hisingerite from Indiana University collection		4.4	3.6	2.6			1.5
Synthetic nontronite, 150°C incubated	11.8		3.8	2.7	2.2		
Synthetic nontronite, 95°C incubated	11.8		3.8				
Unreacted synthetic Fe-rich allophane (this study)			3.50	2.60	2.24	1.92	

Table 8 gives peak positions for all materials, unreacted and reacted, examined in the present study. Data for allophane from Wada and Yoshinaga (1969); data for Al-rich allophane from Parfitt (2009); data for synthetic allophane from Rampe et al. (2012); data for iron-coprecipitated allophane from Ossaka et al. (1971); data for hisingerite from Henmi et al. (1980); data for hisingerite from Geelong, Victoria, Australia from Shayan et al. (1988); data for hisingerite from Riddarhyttan, Sweden, and Gillinge, Sweden from Eggleton and Tilley (1998); data for hisingerite from Indiana University collection from Milliken and Bish (2014); data for synthetic nontronites incubated at 150°C and 95°C from Baker and Strawn (2014)

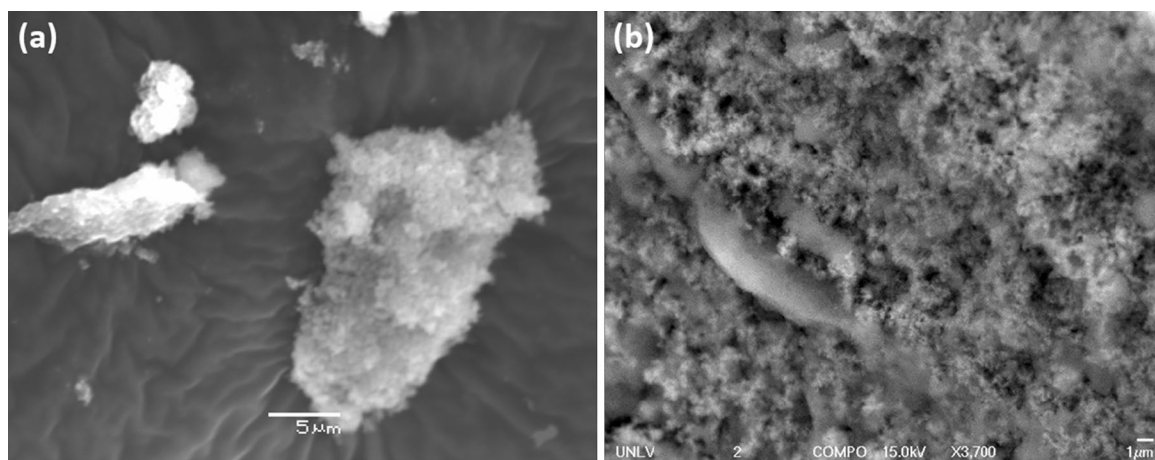


**Fig. 3** Synthetic Fe-rich allophane imaged by **a** SEM and **b** FE-SEM. Nano-spherules are distinguishable in the ‘fluffy’ texture of the aggregate. Similar textures were observed in Fe-free allophane and Fe-poor allophane samples (Figs S6–S7). The long, apparently smooth object in **b** is a ridge of ‘fluffy’ material that is out of focus

mid- to long-range order. Synthetic Fe-free allophane showed no lattice fringes, however, even when exposed to the electron beam for several minutes (Fig. 4e–f). Two different textures were also observed in the Fe-free allophane sample; one ‘rugged’ and one ‘blobby’ (e.g. Figure 4d). A similar textural dichotomy has previously been observed in hisingerite-like, poorly crystalline Si-Fe materials (e.g. Decarreau et al. 1987). Based on observations of a similar texture in the altered Fe-free allophane, the ‘blobby’ texture is probably more hydrated than the ‘rugged’ texture. Only the ‘rugged’ texture was observed in the Fe-rich allophane. These morphologies are consistent with those presented by Wada (1989) for natural allophane and by Eggleton and Tilley (1998) for natural hisingerite.

**BET Surface Area and Particle-size Analysis.** The average BET SSA and particle sizes for unaltered Fe-free allophane, Fe-poor allophane, and Fe-rich allophane are given in Table 1. The average BET SSA for each material was used to normalize the initial dissolution rates to surface area. The BET surface area is not a perfect measurement of reactive surface area, however (Gautier et al. 2001; Velbel 1993), especially in the case of materials with large internal surface areas, such as allophane. Additionally, due to the tendency for allophane to form large aggregates consisting of hollow, porous nano-spheres (e.g. Figure 3; Abidin et al. 2004), the particle sizes reported here represent the mean sizes of aggregate “grains” of each material, which help to explain the apparent discrepancy between large particle sizes and large surface areas. The complete results of particle-size analyses and BET SSA analyses are given in Table S2.

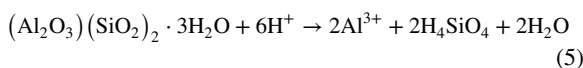
**Total digestions.** Comparison of digestion data with predicted compositions of the unaltered materials from the

formulae indicated additional water present in the synthesized phases, either structural or adsorbed, as well as the phases potentially being enriched in Al (Table 6). The compositions of synthetic Fe-free allophane and Fe-poor allophane are similar to some natural samples, and synthetic Fe-rich allophane is similar to certain synthetic hisingerites used in other studies (e.g. Baker and Strawn 2014), although it is more Al-rich than most natural hisingerite samples and the Mars amorphous component, and more Fe-rich than most natural allophane samples (Tables 4, S3–S6).

#### Dissolution Experiments

**Solution chemistry.** For all experiments, an initial rapid linear change in pH occurred (Fig. 5), which then leveled off to a steady pH value ( $\text{pH}_{\text{steady}}$ ), corresponding to a stage in which a lack of change in solution chemistry was observed (Fig. S8, Data Sheets S1–S38). The average pH of the linear release stage was calculated and used as the pH of the experiment for calculation of the rate constant (see the Calculations section). The initial and final pH data for the linear release stage of dissolution are summarized in Table 3.

The production or consumption of  $\text{H}^+$  during dissolution of Fe-free allophane, Fe-poor allophane, and Fe-rich allophane can explain the observed pH trends, as well as the potential for formation of secondary phases. For example, the dissolution of Fe-free allophane at  $\text{pH}_0$  3 is described by the reaction:



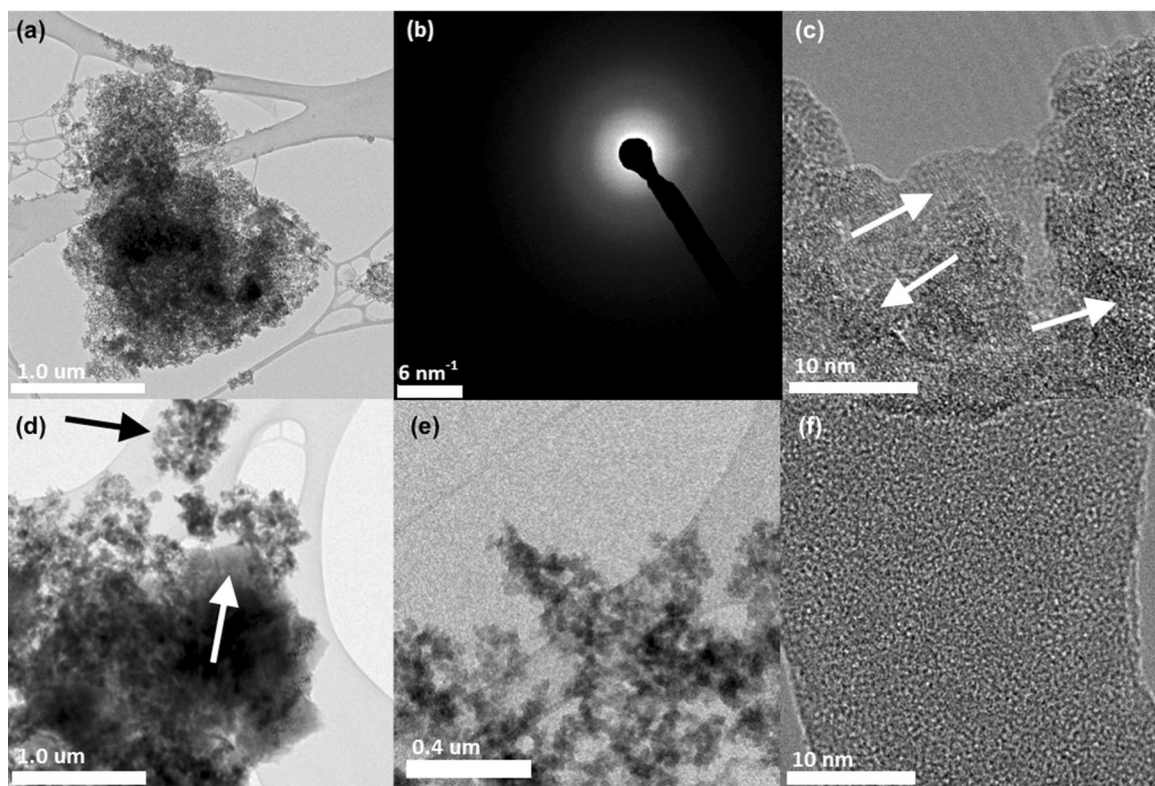
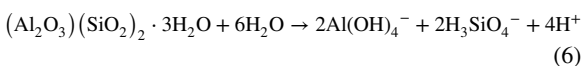


**Fig. 4** FE-STEM images of: **a–c** synthetic Fe-rich allophane and **d–f** Fe-free allophane. **a** Agglomerate of synthetic Fe-rich allophane. **b** Diffraction pattern from an agglomerate of unaltered synthetic Fe-rich allophane, obtained during TEM investigations. Diffuse rings are visible, indicating a nanocrystalline structure. Diffractograms were not obtained for synthetic Fe-free allophane due to its lack of lattice fringes, indicating no long-range order. **c** A very high-magnification view of synthetic Fe-rich allophane. Lattice fringes (arrows) indicate some crystalline structure. **d** An agglomerate of synthetic Fe-free allophane. Nano-spherule-like structures are visible along the edges of the agglomerate. Both the ‘rugged’ (black arrow) and ‘blobby’ (white arrow) textures are visible. **e** A closer view of **d**, showcasing the ‘rugged’ nano-spherule structures. **f** Very high magnification of synthetic Fe-free allophane. Note the lack of lattice fringes, indicating no long-range crystal structure

where  $H^+$  ions are consumed, driving the increase in pH with time observed in the  $pH_{0\_3\_FFA}$  experiment. At  $pH_0$  10, the dissolution of Fe-free allophane is described by the reaction:



where  $H^+$  ions are produced, driving the decrease in pH with time observed in the  $pH_{0\_10\_FFA}$  experiment. The relationship between predicted production and consumption of  $H^+$  ions and observed changes in pH in these experiments was consistent across the range of pH conditions studied (Supplementary Material, Section S8). Although dissolution was not stoichiometric, the general trends described by the equations held true; namely, that the predicted production and uptake of  $H^+$  ions during Fe-rich allophane dissolution was less than that predicted during Fe-free allophane and Fe-poor allophane dissolution. The scatter in the experimental rate data was probably due to the small dependence of silica release rate on pH and possibly

also due to pH change during the experiments (Figs 5 and S8).

Fe remained below the practical quantitation limit of the atomic absorption spectrometer ( $<0.2 \text{ mg L}^{-1}$ ) throughout the duration of the experiment in all experiments except  $pH_{0\_3\_FRA}$ . Iron concentration in solution in the  $pH_{0\_3\_FRA}$  experiment first increased rapidly, then decreased more slowly (Figs 1a, S9). Likewise, Al was only above the practical quantitation limit ( $1.0 \text{ mg L}^{-1}$ ) in the  $pH_0$  3 experiments, probably because these were the only experiments where the pH remained below  $\sim 5$  for the duration of the experiment, and Al precipitation is expected near or above  $pH \sim 5$ . Al concentration in the  $pH_0$  3 experiments first rose rapidly, and then leveled off or decreased slowly as the pH approached  $pH_{\text{steady}}$ , similar to the behavior of Fe in these solutions (Figs 1a, S10).

For all experiments, Si concentrations were above the practical quantitation limit ( $0.2 \text{ mg L}^{-1}$ ) at all time points (Figs 1a, S11–S14), and changes in Si concentrations were similar to trends in pH. Initially, dissolved Si concentrations increased

**Table 6** Compositions in wt.% oxide of unaltered and altered Fe-free allophane, Fe-poor allophane, and Fe-rich allophane determined by ICP-MS analysis of total digestion products (for SiO<sub>2</sub>, Al<sub>2</sub>O<sub>3</sub>, and Fe<sub>2</sub>O<sub>3</sub>) and thermal gravimetric analysis (TGA; for H<sub>2</sub>O) compared with samples from the literature and the approximate values expected from the chemical formulae

Sample	SiO <sub>2</sub>	Al <sub>2</sub> O <sub>3</sub>	Fe <sub>2</sub> O <sub>3</sub>	H <sub>2</sub> O	Sum
Fe-free allophane (formula)	39.1 ± 6.0	41.0 ± 4.1	0	19.9 ± 2.6	100 ± 7.7
Silica Springs	33.4	43.8	0.28		
Unaltered allophane	30.2 ± 1.0	32.2 ± 0.8	ND	36.2 ± 1.0	98.6 ± 1.6
pH <sub>0_3</sub> _FFA	30.4 ± 0.6	36.6 ± 0.9	ND		
pH <sub>0_5</sub> _FFA	30.5 ± 0.2	31.9 ± 0.6	ND		
pH <sub>0_7</sub> _FFA	30.2 ± 1.3	38.3 ± 1.5	ND		
pH <sub>0_10</sub> _FFA	29.9 ± 0.2	37.4 ± 0.3	ND		
Fe-poor allophane (formula)	39.0 ± 6.0	40.5 ± 4.0	0.64 ± 0.06	19.8 ± 2.5	99.9 ± 7.6
Kanumatsuchi	29.17	33.81	0.56		
Unaltered Fe-allophane	29.6 ± 0.7	28.0 ± 0.9	0.47 ± 0.01	36.8 ± 1.0	94.9 ± 1.5
pH <sub>0_3</sub> _FPA	28.9 ± 0.6	33.3 ± 0.9	0.48 ± 0.02		
pH <sub>0_5</sub> _FPA	30.4 ± 1.1	30.0 ± 0.4	0.44 ± 0.01		
pH <sub>0_7</sub> _FPA	28.2 ± 1.0	41.4 ± 0.9	0.39 ± 0.02		
pH <sub>0_10</sub> _FPA	30.1 ± 0.6	37.2 ± 0.2	0.43 ± 0.01		
Fe-rich allophane (formula)	35.1 ± 5.7	18.4 ± 1.6	28.7 ± 2.6	17.8 ± 2.2	100 ± 6.8
Hisingerite	27.5	5.5	51.5		
Unaltered Fe-rich allophane	30.2 ± 0.4	17.5 ± 0.3	19.3 ± 0.5	33.4 ± 1.1	100.4 ± 1.3
pH <sub>0_3</sub> _FRA	28.1 ± 0.6	16.5 ± 0.1	19.7 ± 0.3		
pH <sub>0_5</sub> _FRA	28.8 ± 0.9	18.5 ± 0.7	19.4 ± 0.1		
pH <sub>0_7</sub> _FRA	27.2 ± 0.7	16.8 ± 0.7	19.2 ± 0.5		
pH <sub>0_10</sub> _FRA	28.5 ± 1.0	17.4 ± 0.4	19.3 ± 0.3		

Error in the 'formula' phases was determined by comparing variable Si, Al, Fe, and H<sub>2</sub>O contents in endmember compositions. Error in the analyzed samples represents the standard deviation between two runs of each sample. TGA was not conducted on altered samples because insufficient sample mass was available for analysis. Comparisons of the composition of each unaltered synthetic material with multiple samples from the literature are given in Tables S3–S5

ND = not detected

Data for Silica Springs from Theng et al. (1982); data for Kanumatsuchi from Kitagawa (1974); data for hisingerite from Hisinger (1828)

linearly (e.g. Figure 1b), and then leveled off gradually to steady concentrations of ~0.2–0.5 mM within 18 days.

Dissolution of Fe-free allophane, Fe-poor allophane, and Fe-rich allophane was non-stoichiometric at pH<sub>0</sub> 3. During the pH<sub>0\_3</sub>\_FRA experiment, Fe release was always below the ~0.5:1 stoichiometric formula Fe/Si ratio, while Al release was initially greater than the ~0.5:1 stoichiometric formula Al/Si ratio, and then decreased with time to approximately stoichiometric formula values (Fig. 6). The pH<sub>0\_3</sub>\_FFA and pH<sub>0\_3</sub>\_FPA experiments also showed Al/Si ratios in solution that were initially above stoichiometric formula values and then decreased to below the ~1:1 stoichiometric formula value (Fig. 6). Determination of whether dissolution at pH<sub>0</sub> 5, 7, and 10 was stoichiometric was not possible because dissolved Fe and Al remained below the practical quantitation limit of the AA spectrometer throughout these experiments; low concentrations in solution could have been due to precipitation of secondary

phases or adsorption of Fe<sup>3+</sup> and Al<sup>3+</sup> onto surfaces. Solution chemistry for each time point for each experiment is reported in the Supplementary Material (Section S10).

*Rate law.* Surface area-normalized dissolution rate laws ( $r_{\text{diss}}$ , Eq. 3) were  $\log r_{\text{diss}} = -10.65 - 0.15 \times \text{pH}$  for Fe-free allophane,  $\log r_{\text{diss}} = -10.35 - 0.22 \times \text{pH}$  for Fe-poor allophane, and  $\log r_{\text{diss}} = -11.46 - 0.042 \times \text{pH}$  for Fe-rich allophane. Rate laws for each material were plotted along with the measured rate for each experiment (Fig. 7). The pH dependence for all materials was low; for Fe-free allophane,  $n = 0.146 \pm 0.026$ ; for Fe-poor allophane,  $n = 0.222 \pm 0.040$ ; and for Fe-rich allophane,  $n = 0.042 \pm 0.016$ , where the error is the 1 $\sigma$  standard deviation of  $n$ . The pH dependence of Fe-free allophane and Fe-poor allophane dissolution were almost the same within uncertainty, which is not surprising given the structural and compositional similarity of these phases.

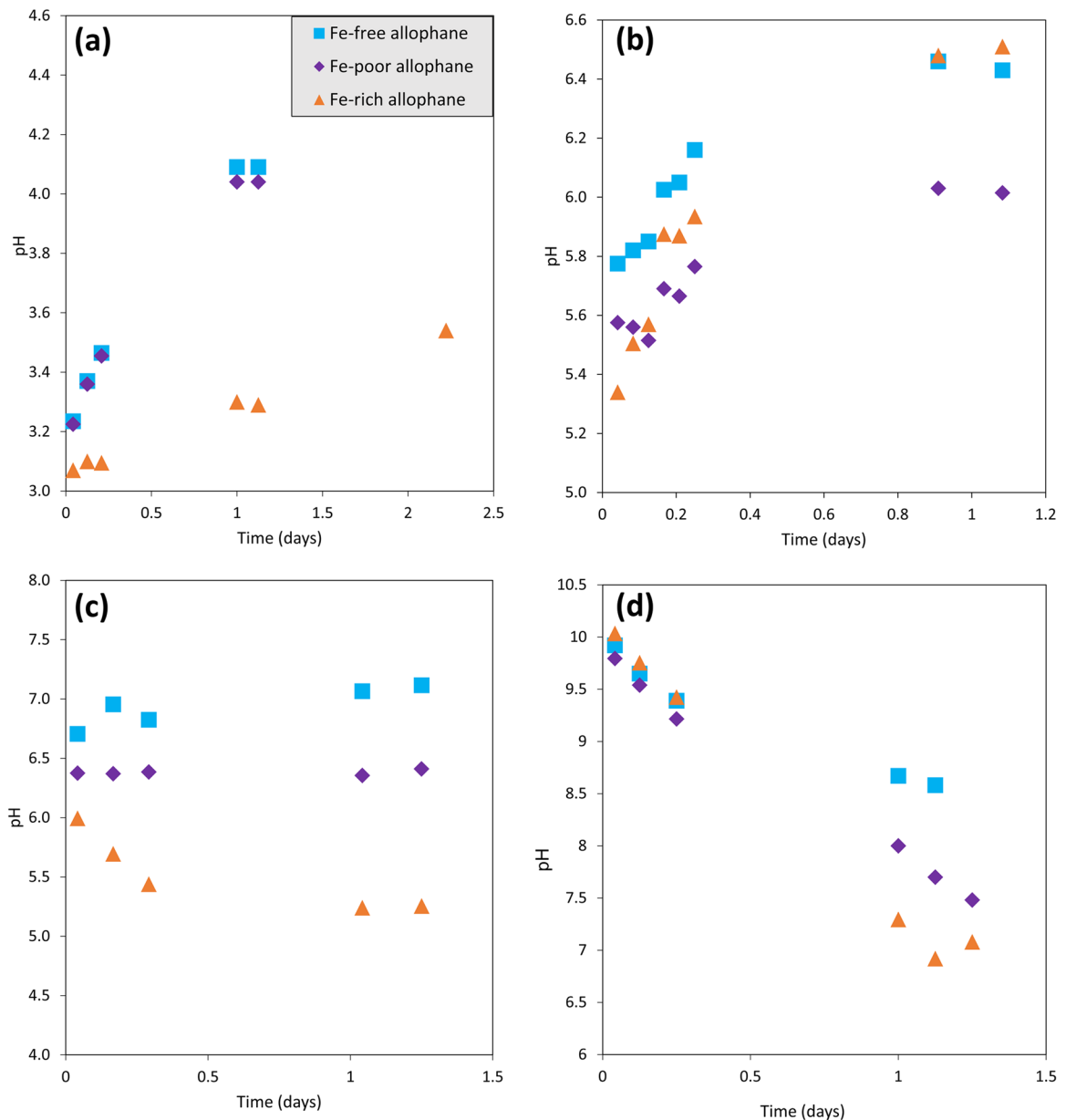


**Fig. 5** Observed change in solution pH with time over the range used to calculate dissolution rates for experiments with **a** pH<sub>0</sub> 3, **b** pH<sub>0</sub> 5, **c** pH<sub>0</sub> 7, and **d** pH<sub>0</sub> 10. Points are the average pH value between two duplicates. Solution pH was measured over the course of the entire experiments (see Fig. S8). Balanced chemical equations (see Supplementary Material, Section S8) explain the observed pH changes

The pH dependence of Fe-rich allophane dissolution was lower than that of the Fe-free allophane and Fe-poor allophane. Similar trends in the pH-dependence of dissolution are observed for Al-rich montmorillonite (e.g. Huertas et al. 2001; Rozalen et al. 2008) and Fe<sup>3+</sup>-rich nontronite (e.g. Gainey et al. 2014), and amorphous Al- and Fe<sup>3+</sup>-phosphates (Tu et al. 2014), with the Fe-rich material showing a lower pH dependence than the Al-rich material

in both cases. Although the water exchange rate around Fe has been shown to be more rapid than that around Al (e.g. Helm and Merbach 2005; Miller et al. 2016), the first hydrolysis constant for Fe<sup>3+</sup> is much larger than that of Al<sup>3+</sup> (Lamb and Jacques 1938; Frink and Peech 1963), which may result in the rapid formation of Fe hydroxides (e.g. Hsu 1976). Additionally, precipitation of Fe-oxide or oxyhydroxide coatings on material surfaces may protect those

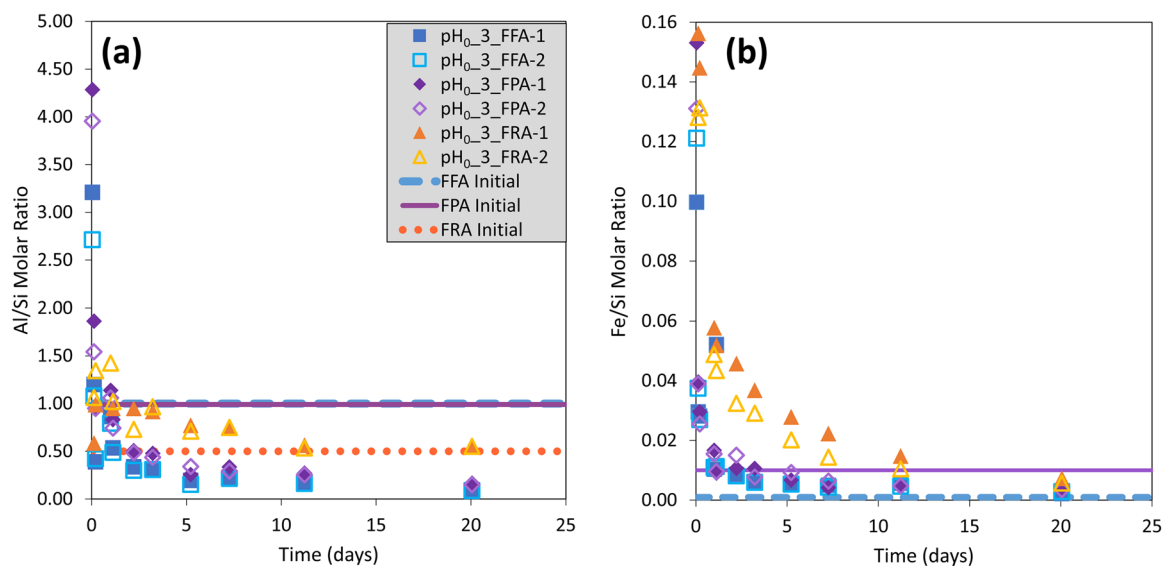


**Fig. 6** **a** Al/Si ratio and **b** Fe/Si ratio measured from solution in pH<sub>0</sub> 3 experiments versus time. Points where Fe, Al, or Si were below detection are not plotted. The formula ratios of the unaltered Fe-free allophane (FFA), Fe-poor allophane (FPA), and Fe-rich allophane (FRA) are indicated by FFA Initial, FPA Initial, and FRA Initial, respectively. In panel **b**, the Fe/Si synthesis ratio of the unaltered Fe-rich allophane is 0.5, well above any of the measured ratios in the solutions studied

surfaces from the surrounding solution and, therefore, slow dissolution of Fe-rich materials compared to Al-rich materials under acidic conditions.

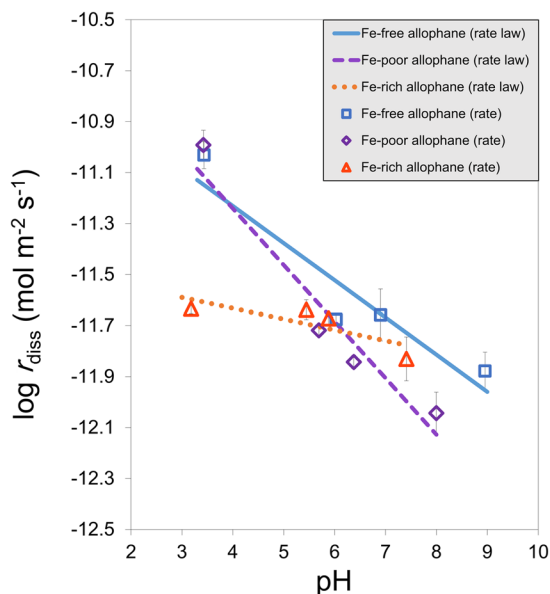


**Fig. 7** Average of the dissolution rates (points) and rate laws calculated as described in the text (lines) for Fe-free allophane, Fe-poor allophane, and Fe-rich allophane at pH<sub>0</sub> values of 3, 5, 7, and 10. Error bars represent the 1 $\sigma$  standard deviation between duplicate experiments. Overall, the pH-dependence of dissolution was low. All experimental data are given in the Supplementary Material

*Particle lifetimes.* Particle lifetimes for Fe-free allophane, Fe-poor allophane, and Fe-rich allophane are given in Table 7. Particle lifetimes were calculated both for a 1  $\mu$ m particle for comparison to literature on other rapidly dissolving phases (e.g. Elwood-Madden et al. 2012; Miller et al. 2016) and using the measured particle size of each unaltered material (Table 1). Particle lifetimes are 0.02–0.18 kyr for a 1  $\mu$ m particle, and 2.5–24.0 kyr for the measured particle sizes. Field dissolution rates of silicate minerals are generally  $\sim$ 2 orders of magnitude slower than laboratory dissolution rates (e.g. Velbel 1993; Zhu et al. 2016), giving a final estimate of between 1.9 and 6.7 kyr for the lifetime of a 1  $\mu$ m allophane particle in moderately acidic waters, and between 10.6 and 18.0 kyr in moderately alkaline waters, consistent with other estimates of the lifetime of martian waters based on the dissolution of rapidly dissolving phases (e.g. Elwood-Madden et al. 2009). Using the measured particle sizes, these estimates extend to 0.3–2.4 Myr. Lower temperatures, higher salinities ( $>$   $\sim$ 0.05 M), and the presence of liquid water intermittently, rather than persistently, would also extend these lifetimes.

An important caveat to these lifetimes is that allophane does not generally form solid spherical particles; rather, it forms loose aggregates that span tens of microns, each made up of hollow, porous nano-spheres  $\sim$ 5–50 nm in diameter (Figs 3 and S6–S7), which may not dissolve according to the shrinking sphere model. Although natural allophane is present in soils up to  $\sim$ 2 kyr old in tropical climates (Bleeker and Parfitt 1974) and in soils  $>$  30 kyr old in more temperate zones (Nagasawa 1978), allophane in these soils may exist as an intermediate material, being simultaneously formed and transformed to more ordered phases or

**Table 7** Particle lifetimes for Fe-free allophane, Fe-poor allophane, and Fe-rich allophane calculated with Eq. 4

Experimental condition	Average $r_{\text{diss}}$ at 25°C $\times 10^{-12}$ (mol m <sup>-2</sup> s <sup>-1</sup> )	Particle size ( $\mu\text{m}$ )	Particle lifetime (kyr)
pH <sub>0</sub> _3_FFA	9.30 $\pm$ 3.74	1.00	0.020 $\pm$ 0.008
		167.5 $\pm$ 2.2	3.35 $\pm$ 1.35
pH <sub>0</sub> _3_FPA	10.20 $\pm$ 4.50	1.00	0.019 $\pm$ 0.008
		133.1 $\pm$ 0.8	2.53 $\pm$ 1.12
pH <sub>0</sub> _3_FRA	2.33 $\pm$ 0.15	1.00	0.067 $\pm$ 0.004
		166.5 $\pm$ 4.9	11.226 $\pm$ 0.82
pH <sub>0</sub> _10_FFA	1.32 $\pm$ 0.02	1.00	0.118 $\pm$ 0.002
		167.5 $\pm$ 2.2	19.747 $\pm$ 0.417
pH <sub>0</sub> _10_FPA	0.95 $\pm$ 0.19	1.00	0.180 $\pm$ 0.038
		133.1 $\pm$ 0.8	24.008 $\pm$ 5.020
pH <sub>0</sub> _10_FRA	1.48 $\pm$ 0.02	1.00	0.106 $\pm$ 0.002
		166.5 $\pm$ 4.9	17.598 $\pm$ 0.586

The molar volume of all allophanes was assumed to be  $1.01 \times 10^{-4}$  m<sup>3</sup> mol<sup>-1</sup>. Error (where given) represents the 1 $\sigma$  standard deviation between duplicates

dissolved, potentially in different zones of the soil. Regions where allophane is present would then represent an environment where the accumulation rate of allophane is equal

to or greater than the rate at which allophane is transformed or dissolved, and not necessarily regions where allophane particle lifetimes are tens of thousands of years.

**Table 8** Calculated peak positions for unreacted Fe-free allophane, Fe-poor allophane, and Fe-rich allophane, and for the altered materials from experiments with pH<sub>0</sub> values of 3, 5, 7, and 10. Numbers in italics are from minor peaks

Material	Peak positions ( $\text{\AA}$ )				
Unaltered allophane	12.27	4.35	3.39	2.25	
pH <sub>0</sub> _3_FFA	11.72	4.37	3.42	2.26	
pH <sub>0</sub> _5_FFA	23.7		3.41	2.25	
pH <sub>0</sub> _7_FFA*	10.82	4.32	3.39	2.27	
pH <sub>0</sub> _10_FFA	11.62	4.29	3.38	2.26	
Unaltered Fe-allophane		4.41	3.42	2.26	
pH <sub>0</sub> _3_FPA	11.07		3.39	2.25	
pH <sub>0</sub> _5_FPA			3.41	2.25	
pH <sub>0</sub> _7_FPA			3.42	2.27	
pH <sub>0</sub> _10_FPA			3.41	2.25	
Unaltered Fe-rich allophane*			3.50	2.24	1.92
pH <sub>0</sub> _3_FRA*			3.47	2.24	
pH <sub>0</sub> _5_FRA			3.47		
pH <sub>0</sub> _7_FRA*			3.45	2.21	
pH <sub>0</sub> _10_FRA*	12.2		3.45	2.24	1.92

\*Quartz contamination from grinding in agate mortar and pestle was observed in the form of a small, sharp peak at 3.34  $\text{\AA}$ . Contamination was more common in Fe-rich samples because the Fe-rich allophane was harder than the other allophanes and required more rigorous grinding

### Characterization of Reacted Materials

**XRD.** Samples of Fe-free allophane, Fe-poor allophane, and Fe-rich allophane from each experiment were examined with XRD to investigate the possible formation of secondary phases. No well crystallized products, such as gibbsite or hematite, were present above the detection limit of the instrument ( $\sim 1$  wt.%); however, a broad, low-angle peak developed as a result of alteration in Fe-free allophane reacted at pH<sub>0</sub> 3, 7, and 10; in Fe-poor allophane reacted at pH<sub>0</sub> 3; and in Fe-rich allophane reacted at pH<sub>0</sub> 10 (Figs 8 and S15). This broad peak occurs near 11–12 Å, larger than the typical (001) *d* spacing for kaolinite ( $\sim 7.2$  Å, Goodyear and Duffin 1961) and smaller than that of type examples of hydrated smectites (13.5–15 Å, Moore and Reynolds 1997), although similar to the (001) peak observed by Pickering (2014) in the partially hydrated SWy-2 Na-montmorillonite (11.8 Å) and certain other samples of montmorillonite (e.g. Klopogge et al. 2002, with *d* spacings of 11.5–15.0 Å). The 11–12 Å peak could alternately be due to the collapse of a smectite-like phase due to exposure to vacuum during freeze-drying (e.g. Frushour and Bish 2017). Therefore, this broad peak may represent the early development of a clay mineral, as also seen in the HRTEM results. The observed peak positions for all reacted and unreacted materials are given in Table 8.

**Microscopy.** Analyses by SEM of pH<sub>0</sub>\_3\_FRA (pH<sub>steady</sub>  $\sim 4$ ) reacted for two days and for one month revealed that the grain texture tended to become more porous with increasing dissolution time, and that the grains themselves

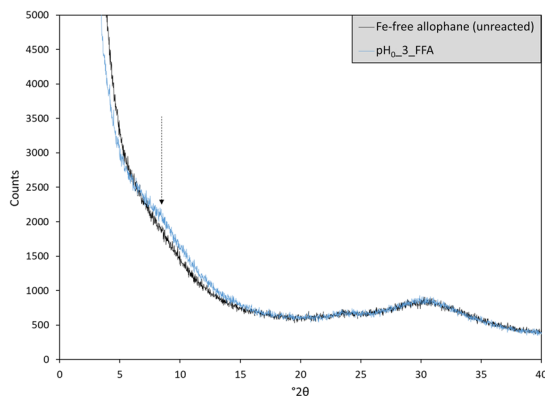


**Fig. 8** XRD patterns of unreacted Fe-free allophane and Fe-free allophane reacted at pH<sub>0</sub> 3 (pH<sub>0</sub>\_3\_FFA), demonstrating the development of a possible phyllosilicate-like precursor phase (arrow) with a peak centered around 12.3 Å. A similar, but less pronounced, feature was observed in Fe-free allophane samples reacted at pH<sub>0</sub> 7 and 10, in Fe-poor allophane reacted at pH<sub>0</sub> 3, and in Fe-rich allophane reacted at pH<sub>0</sub> 10. XRD patterns of all unreacted and reacted materials were collected (see Fig. S15). CoK $\alpha$  radiation was used for all patterns

tended to become smaller (Figs S16–S17), possibly indicating the presence of less ordered material that dissolves more rapidly than the surrounding material, causing disaggregation. Analyses of reacted materials by SEM are summarized in Table S1.

After a 2-month reaction time, pH<sub>0</sub>\_10\_FRA showed the formation of small ( $\sim 2$   $\mu$ m) linear features within the larger Fe-rich allophane aggregates (Figs 9a and S18) in HRTEM analysis (analyses of reacted materials by HRTEM are summarized in Table S7). These features were interpreted as the rolled or curled edges of silicate sheets, possibly due to the incipient conversion to phyllosilicate. Similar features have been observed in synthetic hisingerite-like Si-Fe precipitates, and were also interpreted as the edges of phyllosilicate layers (Decarreau et al. 1987). Overall, the material was still poorly crystalline, and the linear features did not demonstrate a greater degree of crystallinity than the surrounding masses, as demonstrated by their lack of lattice fringes. The linear features were also observed in pH<sub>0</sub>\_3\_FRA reacted for 6 months, although they were much less prevalent (Fig. S19). In contrast, no linear features were observed in unaltered Fe-rich allophane.

Only a few of these linear “edge-curl” features were observed in pH<sub>0</sub>\_10\_FFA reacted for 2 months (Fig. S20). Fe-free allophane also maintained the morphological dichotomy between a ‘rugged’ texture and a ‘blobby’ texture (Fig. 9b) seen in the unreacted material. The ‘blobby’ texture was rapidly destroyed by the high-energy STEM beam, while the ‘rugged’ texture was more robust, suggesting a higher degree of hydration in the ‘blobby’ material (Fig. S21; Decarreau et al. 1987). This extreme beam sensitivity was only observed directly in the altered Fe-free allophane but may also be true of the unaltered Fe-free allophane. No ‘blobby’ material was observed in the altered or unaltered Fe-rich allophane samples.

**Total digestion.** Changes in bulk chemistry due to dissolution are given in Table 6. Total digestions showed that SiO<sub>2</sub> was released preferentially from some samples (e.g. pH<sub>0</sub>\_7\_FPA), while others (e.g. pH<sub>0</sub>\_7\_FFA) maintained relatively stable SiO<sub>2</sub> content. The amount of SiO<sub>2</sub> released during dissolution of Fe-rich allophane correlated well with the change in bulk SiO<sub>2</sub> content measured by total digestion (Fig. S22). Neither Fe-poor allophane nor Fe-rich allophane showed detectable differences in Fe<sub>2</sub>O<sub>3</sub> between experimental conditions and the unreacted samples. The observed enrichment in Al<sub>2</sub>O<sub>3</sub> in some samples (e.g. pH<sub>0</sub>\_10\_FFA) was due to a net loss of SiO<sub>2</sub> from the samples. This was corroborated by the pH<sub>0</sub>\_7\_FPA experiment, where the greatest net loss of SiO<sub>2</sub> ( $\sim 1$  wt.% versus the unreacted sample) was accompanied by the greatest enrichment in Al<sub>2</sub>O<sub>3</sub> ( $\sim 12$  wt.% versus the unreacted sample). No correlation between SiO<sub>2</sub> loss and Al<sub>2</sub>O<sub>3</sub> enrichment or loss was observed in the Fe-rich allophane samples.



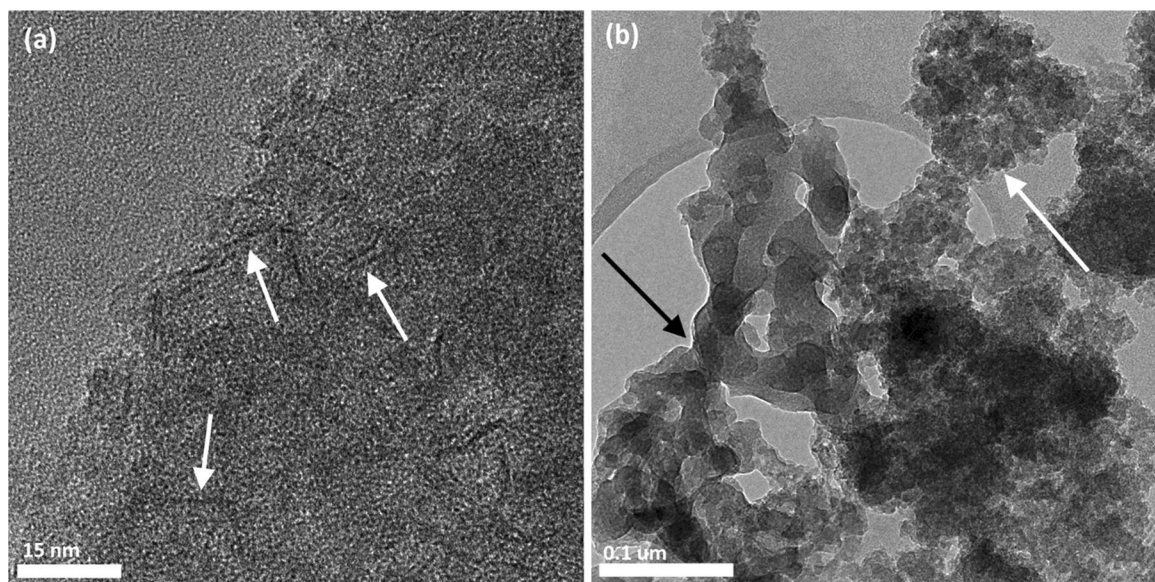


**Fig. 9** FE-STEM images of **a** synthetic Fe-rich allophane and **b** synthetic Fe-free allophane, each reacted at  $\text{pH}_{\text{steady}}$  values of  $\sim 8$  ( $\text{pH}_0$  10) for 57 days. Edge-curl features were much less prevalent in the Fe-free allophane sample than in the Fe-rich allophane (see Fig. S20 for an example of an edge-curl feature in the Fe-free allophane). **a** Arrows indicate linear features that may represent the curled edges of incipient phyllosilicate-like sheets. **b** The ‘blobby’ morphology is visible on the left (black arrow), while the ‘rugged’ morphology is on the right (white arrow)

## DISCUSSION.

### *Comparison of Synthetic and Martian Amorphous Materials*

Comparison of synthetic materials with phases found on the martian surface is necessary to ensure that they are appropriate functional analogs. These synthetic analogs can help elucidate properties of the amorphous component in martian rocks and soils that cannot be examined with current remote instrumentation, such as dissolution kinetics, micro-morphology, and formation of secondary phases.

The XRD patterns of synthesized Fe-free allophane, Fe-poor allophane, and Fe-rich allophane all have broad peaks centered around  $2\theta$   $\text{CoK}\alpha$  (3.39–3.5 Å, Fig. 2b, Tables 5 and 8), similar to the amorphous humps in the CheMin patterns of samples from Gale crater (Fig. 10), including the Rocknest ‘soil’ sample and the Cumberland, John Klein, and Windjana rock samples (Bish et al. 2013; Achilles et al. 2017). Mass-balance calculations (e.g. Dehouck et al. 2014; Vaniman et al. 2014; Morrison et al. 2018; Achilles et al. 2017; Rampe et al. 2018) provided a range of possible compositions for the martian amorphous component, bearing in mind that the compositions may be slightly skewed by the presence of crystalline phases in abundances below the CheMin detection limit (e.g. Smith et al. 2018; Rampe et al. 2020; Table S6). The Al contents of the synthesized Fe-free allophane, Fe-poor allophane, and Fe-rich allophane are much greater than that of the martian amorphous component (Table S6), which may be due to the presence

of other high-silica and high-Fe phases, such as high-silica glasses (e.g. 72.5 wt.%  $\text{SiO}_2$ , 9.36 wt.%  $\text{Al}_2\text{O}_3$ , 0.95 wt.% FeO; Beard et al. 2015) and/or opaline silica, Fe oxides, and Fe sulfates in the martian samples (Achilles et al. 2017; Rampe et al. 2017). Alternatively, Al-rich amorphous materials, such as allophane, may simply not be present in the Mars amorphous material. The large Fe and Si contents of the martian material indicate that hisingerite ( $\sim 33.5$  wt.% Fe,  $\sim 16.8$  wt.% Si; Henmi et al. 1980) or a co-occurrence of ferrihydrite and amorphous silica are plausible component phases (Dehouck et al. 2017).

The EGA data of the synthetic samples used in this study (Figs S3–S4) were dominated by water release at  $\sim 130$ – $400^\circ\text{C}$ . The SAM data from the Rocknest, Cumberland, John Klein, and Windjana samples in Gale crater showed  $\text{H}_2\text{O}$  release primarily between  $100$ – $450^\circ\text{C}$ , probably including releases from hydrated sulfates and clay minerals (Leshin et al. 2013; Sutter et al. 2017). The study by Sutter et al. (2017) predicted adsorbed water release, perhaps due to allophane and other amorphous phases, below  $\sim 200^\circ\text{C}$ , and that by Leshin et al. (2013) attributed water release from martian samples at  $\sim 110^\circ\text{C}$  to allophane. These values ( $\leq 200^\circ\text{C}$  and  $\sim 110^\circ\text{C}$ ) are consistent with the measured release at  $\sim 130$ – $400^\circ\text{C}$  from the samples examined in the present study. Although only a small fraction of the water release from samples at Gale crater is attributed to amorphous materials, measurements from these synthetic allophanes agree well with that fraction.

Based on current data and the results of XRD, total chemistry, and EGA analyses, therefore, synthetic Fe-free

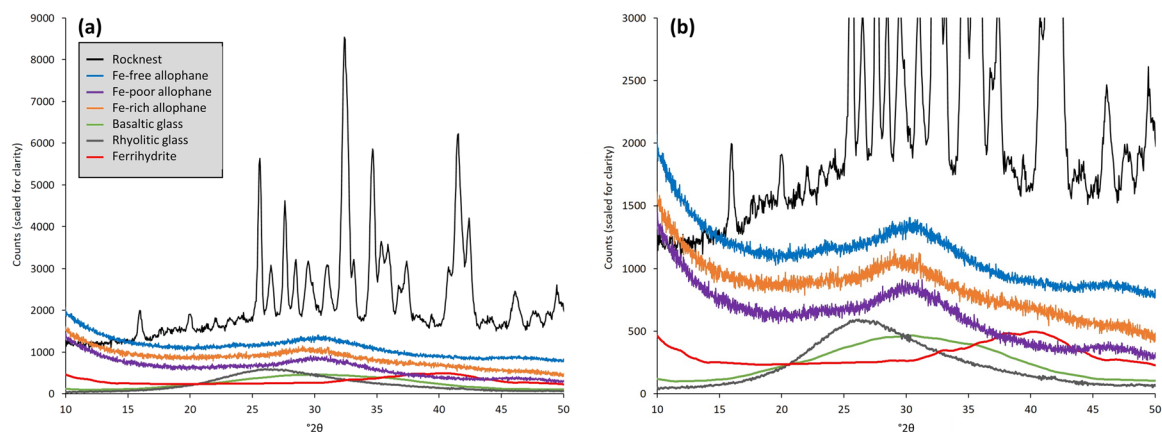


**Fig. 10** Comparison of the XRD patterns of synthetic Fe-free allophane, Fe-poor allophane, and Fe-rich allophane with a 2-line ferrihydrate from the *FULLPAT* library and the CheMin XRD pattern from the Rocknest soil sample. Panel **a** shows the full patterns, and panel **b** is zoomed in to better demonstrate the concordance between amorphous materials from the present study and the amorphous humps in the Rocknest pattern. CoK $\alpha$  radiation was used for all patterns

allophane, Fe-poor allophane, and Fe-rich allophane are appropriate analogs for at least portions of the amorphous component in modern martian soils and ancient sedimentary rocks and can be used to help understand better these amorphous materials.

#### Dissolution Rates and Rate Laws

The dissolution rates measured for Fe-free allophane, Fe-poor allophane, and Fe-rich allophane are within 10% of each other (Fig. 7) and are approximately an order of magnitude faster than dissolution rates of crystalline clay minerals of similar compositions, such as nontronite (Gainey et al. 2014; Steiner et al. 2016) and montmorillonite (e.g. Huertas et al. 2001; Rozalen et al. 2008) (Fig. 11). This trend is consistent with trends observed for other amorphous or poorly crystalline materials; amorphous Al and Fe phosphates dissolve more rapidly than crystalline Al and Fe phosphates (Huffman 1960; Tu et al. 2014), and amorphous silica dissolves more rapidly than quartz (Liang and Readey 1987). The surface area-normalized dissolution rates measured for Fe-free allophane, Fe-poor allophane, and Fe-rich allophane, however, are similar to those measured for goethite at pH~3 (Cheah et al. 2003), amorphous silica at pH~3 (Icenhower and Dove 2000), and alunite at pH~3–5 (Miller et al. 2016) at the same pH values, and are slower than the surface area-normalized dissolution rates measured for basaltic glass (Gislason and Oelkers 2003) and jarosite (Elwood-Madden et al. 2012) across the pH range (Fig. 11a). Based on the surface area-normalized dissolution rates, interactions between liquid water and poorly crystalline silicate phases, such as allophane and hisingerite, release cations and silica into solution more rapidly than well crystalline silicate phases with similar compositions (especially when polymerized Si is present in the interior of the allophane or hisingerite nano-spherules), but at rates similar to or slightly slower than well crystalline Fe/

Al-sulfates and Fe-oxides and amorphous silica. The samples used in the present study, however, have very large BET surface areas (380–510 m<sup>2</sup> g<sup>-1</sup>, Table 1) and BET surface area is not a perfect proxy for reactive surface area (e.g. Gautier et al. 2001). For example, in both martian and terrestrial environments, mineral dissolution is probably affected by the surface area accessible to water, which may be affected by the size of allophane aggregates (Karube et al. 1996) or armoring of allophane surfaces by secondary precipitates. To account for the very large specific surface areas of these materials, the measured dissolution rates were also normalized to the mass of material in the reactor (Fig. 11b). The mass-normalized dissolution rates of these synthetic materials are faster than those of montmorillonite, nontronite, goethite, and basaltic glass, and are similar to those of amorphous silica, alunite, and jarosite.

A low pH dependence was observed for dissolution of all materials in the initial pH range from 3 to 10 (Fe-free allophane,  $n=0.145 \pm 0.028$ , Fe-poor allophane,  $n=0.222 \pm 0.040$ , and Fe-rich allophane,  $n=0.042 \pm 0.016$ ). These dependences are much lower than for other silicates with similar compositions; e.g. for montmorillonite,  $n=0.34$ , and nontronite,  $n=0.297$ , under acidic conditions (Huertas et al. 2001; Gainey et al. 2014). Based on dissolution experiments with naturally occurring allophane, conducted by Abidin et al. (2004), the pH dependence of allophane dissolution probably increases dramatically above pH~10, similar to the trend observed in the pH dependence of kaolinite dissolution ( $n_{\text{OH}^-}=0.472$ , Palandri and Kharaka 2004 and references therein). In both materials, this is probably due to the increased solubility of silica and aluminum at high pH.

The dissolution behavior of Fe-free allophane, Fe-poor allophane, and Fe-rich allophane — similar dissolution rates, with low reaction orders with respect to pH — may be explained by the structures of allophane and hisingerite.

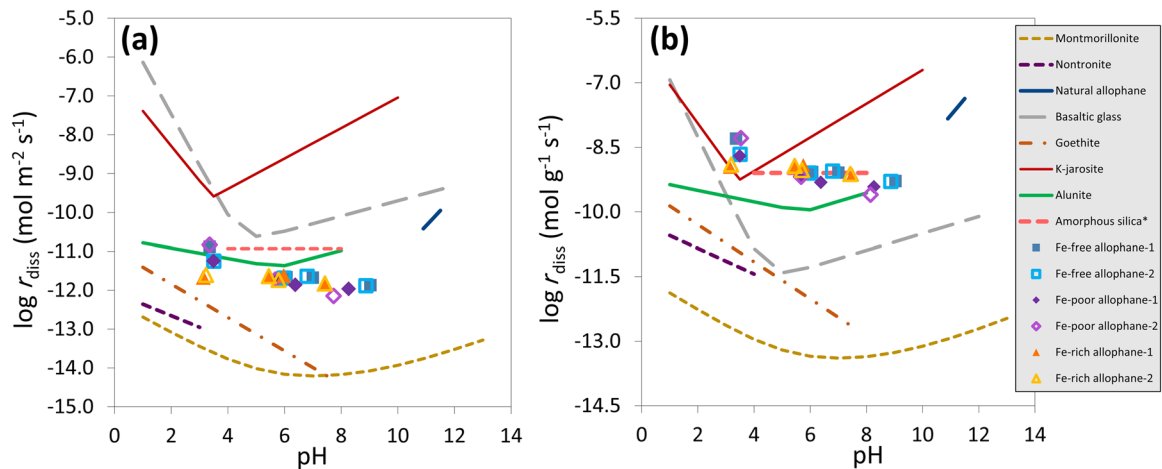


**Fig. 11** Comparison of the log of: **a** the surface area-normalized and **b** mass-normalized dissolution rates of the synthetic Fe-free allophane, Fe-poor allophane, and Fe-rich allophane at 25°C (points) with rate laws for montmorillonite (Rozalen et al. 2008), nontronite (Gainey et al. 2014), natural allophane (Abidin et al. 2004), basaltic glass (Gislason and Oelkers 2003), goethite (Cheah et al. 2003), K-jarosite (Elwood-Madden et al. 2012), alunite (Miller et al. 2016), and amorphous silica\* (Rimstidt and Barnes 1980) (lines) \*modified to reflect elevated dissolution rates in 0.01 M NaCl as per Icenhower and Dove (2000) in order to make a more direct comparison with the conditions of these dissolution experiments. Slower dissolution rates of allophane relative to glass and jarosite in panel **a** may be impacted by the very large surface areas of Fe-free allophane (BET SSA  $\approx$  386 m<sup>2</sup> g<sup>-1</sup>), Fe-poor allophane (BET SSA  $\approx$  350 m<sup>2</sup> g<sup>-1</sup>), and Fe-rich allophane (BET SSA  $\approx$  507 m<sup>2</sup> g<sup>-1</sup>), as evidenced by the mass-normalized rates shown in panel **b**. Error bars are smaller than the points

Allophane consists of hollow, porous nano-spherules  $\sim$ 5 nm (50 Å) in diameter, formed from a rolled silica sheet surrounded by a gibbsite sheet (Iyoda et al. 2012; Wada 1989). Additional polymerized Si is contained in the interior of the nano-spherules when the Al:Si ratio is  $<$ 2:1 (Jeute et al. 2021; Childs et al. 1990; Parfitt 1990). Although gibbsite dissolution has a large reaction order with respect to pH ( $n=0.992$ ) (Palandri and Kharaka 2004), dissolution of pure silica phases, such as amorphous silica, does not depend on pH (e.g. Palandri and Kharaka 2004). Dissolution rates based on Si release rates would be expected to be relatively insensitive to pH because the interior polymerized Si can enter solution through the nano-spherule pores regardless of the rate at which the gibbsite layer is dissolved. In the high-acidity experiments (pH<sub>0</sub> 3), an initial preferential leaching of Al was observed, consistent with the rapid dissolution of an Al-rich layer, and little variation in dissolution rate based on silica release rate was observed across the range of pH conditions, consistent with the mostly independent dissolution of interior silica.

A similar layered nano-spherule structure was observed in hisingerite (Shayan 1984; Eggleton and Tilley 1998) and may also exist in Fe-rich allophane. The hisingerite layers occur in multiple concentric sheets, however, similar to the structure of true phyllosilicates, and form nano-spherules up to 200 Å in diameter (Shayan 1984). These multiple concentric layers may reduce the dissolution rate under acidic conditions by protecting the interior of the spherules from protons in solution. Precipitation of Fe-oxide phases on the surface of hisingerite particles might also inhibit

further dissolution by blocking pores or access to surface sites. The dissolution reactions of these synthetic allophanes (e.g. Eq. 5, Section S8) also help explain the lower pH dependence of Fe-rich allophane than the Fe-free and Fe-poor allophanes by demonstrating the reduced consumption/production of H<sup>+</sup> by Fe-rich allophane versus Fe-free allophane and Fe-poor allophane.

Release of Fe and Al from synthetic materials in this study was approximately equal to or below stoichiometric values with respect to Si (Fig. 6), with all Fe:Si and Al:Si ratios below stoichiometric values when pH<sub>steady</sub> was reached. This non-stoichiometric dissolution indicates that the altered material is probably more Al- and Fe-rich than the starting material, as supported by chemical composition of the reacted samples (Table 8). Aluminum (and Fe if present) is first leached rapidly from the gibbsite sheet in the nano-spherules (Data Sheets S29–S38), and then may be reprecipitated or adsorbed, as indicated by the decrease in solution concentrations of Al and Fe with time.

#### Secondary Phases and Altered Material

Allophane and hisingerite are considered generally to occur as intermediates in the formation of more stable phases, such as kaolinite and nontronite (Wada 1989). Generally, during the weathering process, silica and aluminum or iron can combine to form allophane and/or hisingerite, which are then converted to imogolite or halloysite, and then to more mature layer silicates (Wada 1989). Despite the studies examining these large-scale transitions, however, little work has been done to examine the incipient weathering of

poorly crystalline phases such as allophane and hisingerite (e.g. Farmer et al. 1991; Farmer 1997). The current study showed that under alkaline conditions, layered, phyllosilicate-like precursor materials formed rapidly (on the order of a few months) from Fe-free and Fe-rich allophane under laboratory conditions, in agreement with previous work by Farmer et al. (1991) and Farmer (1997), which examined weathering of hisingerite under high temperatures and in calcareous conditions at both high and low temperatures.

FE-STEM analyses of pH<sub>0\_10\_FRA</sub> reacted for 2 months (pH<sub>steady</sub> ~ 8) showed linear ‘edge-curl’ features that were not present in the unreacted materials (Figs 4a, 4c, 9a, S18). At low pH, fewer of these linear features were observed (Fig. S19). This observation supports the XRD data that indicated incipient phyllosilicate formation from Fe-rich allophane is less favorable at low pH than at alkaline pH.

As described above, Fe-free allophane and Fe-poor allophane show fewer phyllosilicate-like ‘edge-curl’ features than Fe-rich allophane when reacted under alkaline pH conditions for 2 months (Figs S20–S21). The Fe-rich allophane may behave differently from the Fe-poor and Fe-free allophanes because of reprecipitation or reduced dissolution of the Fe-containing material, as evidenced by the decrease in Fe concentration in solution with time (see Figs 1, 6, S9). Reprecipitated Fe-containing material, in combination with the silica-rich solution generated during alteration at alkaline pH, may create a favorable environment for incipient phyllosilicate characteristics to develop, similar to the formation of framework layers containing silica and divalent/trivalent cations during the synthesis of nontronite and saponite by the sol–gel method (e.g. Harder 1976, 1978; Baldermann et al. 2014; Gainey et al. 2017) and the formation of some seafloor nontronites (Sun et al. 2011). Because the Fe-free and Fe-poor allophane lack significant Fe, they may be less likely to develop phyllosilicate precursor phases when exposed to alkaline Si-containing solutions.

The bulk chemistry of unreacted and reacted samples (Table 6) shows that some reacted samples underwent a net loss of Si versus the unreacted sample, while others did not. A net loss of Si was observed in Fe-rich allophane samples across the range of pH conditions studied here, although no clear correlation was found between net Si loss and the pH of the experiment. A net loss of Si was also observed in the pH<sub>0\_7\_FPA</sub> experiment. No appreciable differences in Si content were observed between any of the Fe-free allophane samples. This observation indicates that the Si that dissolved from all of the Fe-free allophane experiments and all but one of the Fe-poor allophane experiments either: (1) reprecipitated before the end of the experiment (but was not detectable via XRD or microscopy); or (2) did not dissolve in sufficient quantity to produce a detectable change in Si content of the final reacted material. Similarly, for the Fe-rich allophane experiments (and pH<sub>0\_7\_FPA</sub>), Si may have dissolved in sufficient quantities to detectably affect the composition of the remaining solids, and not reprecipitated in sufficient quantities to erase the signature of its

dissolution. The amount of Si released into solution during dissolution experiments and the amount of Si remaining in each sample was plotted to illustrate this relationship (Fig. S22).

#### *Implications of Experiments for Mars*

The dissolution experiments with Fe-free and Fe-bearing allophane demonstrated rapid initial dissolution and enrichment of Al and Fe across the range of pH conditions. Si in the interiors of Fe-free allophane, Fe-poor allophane, and Fe-rich allophane nano-spherules is accessed through pores in the nano-spherule walls, dissolves rapidly with little dependence on pH, and tends to remain in solution. Aluminum and Fe from the nano-spherule walls may reprecipitate rapidly, readsorb, or not enter solution at all. FE-STEM analyses of reacted materials showed diagnostic linear features (e.g. Fig. 9a) that were not seen in unreacted material, which were more prevalent at alkaline pH than at acidic pH. In the event that samples containing hisingerite or allophane are returned from Mars, similar features that indicate brief interaction with past liquid water (on the order of months to years) may be detectable. The rapid alteration of poorly crystalline silicate materials could be a useful tool for examining very short-lived episodes of water–rock interaction; on timescales where more crystalline silicate materials would show little to no chemical, mineralogical, or structural change due to interaction with water, poorly crystalline silicate materials may be altered significantly. Evidence for limited water–rock interactions captured by poorly crystalline silicate materials in returned martian samples may not capture *in situ* processes, however. Martian samples will be sealed in collection tubes and left on the surface for years before return to Earth. Hydrated materials may dehydrate diurnally or seasonally (e.g. Vaniman et al. 2018), potentially allowing water vapor to condense on particles in the sample tubes. The rapid dissolution rates of Fe-free allophane, Fe-poor allophane, and Fe-rich allophane suggest that these materials may be altered if sufficient water is present during such a scenario and, therefore, samples should be returned rapidly to limit alteration within sample tubes.

The continued presence of allophanic materials in returned samples from Mars could indicate that interactions of liquid water with the amorphous component were limited, consistent with other observations of mineral assemblages in Gale crater (e.g. the co-occurrence of jarosite and fluorapatite, as discussed by Rampe et al. 2017). Although the dissolution rates of all three synthetic materials were fastest at pH<sub>0</sub> 3, and slower at more alkaline pH conditions, the range between the fastest and slowest dissolution rates spans less than an order of magnitude. Therefore, allophane or hisingerite on Mars would have dissolved or altered to more crystalline phases rapidly if abundant liquid water was present, regardless of the water’s pH, although field dissolution rates are expected to be ~2 orders of magnitude slower than the dissolution rates measured in laboratory experiments (e.g. Velbel 1993; Zhu et al. 2016). The temperatures

on Mars, when liquid water was present, were also probably much lower than 25°C, which would further slow dissolution and extend the lifetimes of allophane or hisingerite. Waters with low salt concentrations, such as those that might be found in the “dilute lake waters” that may have filled Gale crater (Rampe et al. 2017), can enhance significantly dissolution of Si-rich phases such as quartz and amorphous silica, however (e.g. Dove and Nix 1997; Icenhauer and Dove 2000). Higher concentrations of salts tend to slow dissolution rates across a range of minerals, with dissolution rates slowing in proportion to decreasing water activity (Pritchett et al. 2012; Olsen et al. 2015; Steiner et al. 2016), and high ionic strength brines, such as those proposed by Tosca et al. (2008) as the global norm throughout most of martian history, could result in significantly reduced dissolution rates and even further extend the lifetimes of rapidly dissolving phases.

Amorphous materials have been found in all samples examined to date in Gale crater, with the relative proportion of amorphous material increasing from ~20 wt.% at the base of Mt. Sharp to >50 wt.% in formations farther up-section (e.g. Frydenvang et al. 2017; Rampe et al. 2017; Yen et al. 2017). The amorphous material in the Pahrump Hills member becomes increasingly silicic as the amount present in samples increases, although this may be due to a more silicic source rock (Morris et al. 2016; Rampe et al. 2017). Likewise, the amount of smectite decreases along the traverse up-section into Pahrump Hills until smectite abundance falls below CheMin’s detection limit, while phases produced by acidic alteration (e.g. jarosite) are sandwiched between the silica-rich and smectite-rich members (Morrison et al. 2018). Little olivine is observed in the rock samples from Gale crater, but olivine is present in greater proportions in the aeolian samples, which are considered to be representative of the bulk Mars crust (e.g. Bish et al. 2013; Blake et al. 2013; Meslin et al. 2013; Morrison et al. 2018). Taken together, these lines of evidence indicate that the rocks in Gale crater have undergone significant in situ chemical alteration (e.g. Yen et al. 2017; Hausrath et al. 2018; Morrison et al. 2018), although the presence of a non-equilibrium mineral assemblage, including jarosite, fluorapatite, and perhaps allophane or hisingerite, indicates that aqueous alteration was either time-limited or occurred in multiple stages, with the later stages being both briefer and more acidic than those that preceded them (e.g. Rampe et al. 2017; Yen et al. 2017; Hausrath et al. 2018).

Based on the proposed chemical composition of the amorphous material and the presence of Fe-rich clay minerals in the stratigraphically lowest mudstones of Gale crater (Cumberland and John Klein), the amorphous material observed in these samples may contain a significant hisingerite component (Dehouck et al. 2017). This hisingerite could represent an intermediate between primary olivine/pyroxene and the smectite clay minerals. These mudstones are the most likely of the samples from Gale crater that have been examined so far to contain hisingerite due to their Fe- and Si-rich compositions, high proportions of clay minerals,

and limited interaction with acidic waters (Dehouck et al. 2014). At the top of the Pahrump Hills member, where the amorphous component is predominantly amorphous silica, no smectites are detected, indicating that either: (1) both the smectites and their precursor phases (i.e. hisingerite) have been dissolved; or (2) no smectites or precursor phases ever formed there. The presence of acid-alteration products and multiple cation deficiencies in these locations point to extensive leaching by acidic groundwater. Acidic groundwaters would be expected to dissolve rapidly any hisingerite that was present in these rocks, producing abundant amorphous silica as a leachate, and the subsequent dissolution of this silica may have been less rapid. A more silicic sediment source may be responsible for the observed silica enrichment in Pahrump Hills (Morris et al. 2016; Rampe et al. 2017), however, with acid alteration playing a more minor role, possibly during late-stage diagenesis.

## CONCLUSIONS

Dissolution experiments with synthetic Fe-free allophane, Fe-poor allophane, and Fe-rich allophane in the range of initial pH<sub>0</sub> 3–10 indicate rapid initial dissolution, approximately an order of magnitude faster than that of well crystalline clay minerals of similar composition. The dissolution rates based on Si release of all three materials showed little pH dependence across the experimental pH range. For Fe-free allophane,  $\log r_{\text{diss}} = -10.65 - 0.15 \times \text{pH}$ ; for Fe-poor allophane,  $\log r_{\text{diss}} = -10.35 - 0.22 \times \text{pH}$ ; and for Fe-rich allophane,  $\log r_{\text{diss}} = -11.46 - 0.042 \times \text{pH}$  at 25°C, where  $r_{\text{diss}}$  has the units of  $\text{mol m}^{-2} \text{s}^{-1}$ . Experimental results indicate that poorly crystalline allophane-like materials in Gale crater would have dissolved rapidly when exposed to liquid water regardless of the water’s pH. The detection of poorly crystalline materials in Gale crater suggests that interaction of liquid water with these materials was limited after the X-ray amorphous materials formed. In the case of more prolonged interactions, the materials would be expected to have either dissolved completely or altered to form more stable phases. Dissolution in Gale crater would probably have proceeded significantly more slowly than in the experiments of the present study, with particle lifetimes on the order of tens of thousands to hundreds of thousands of years, due to the lower temperature and greater salinity expected in the ancient waters of Mars, as well as generally slower dissolution rates in the field than in the laboratory.

Analyses with FE-STEM of reacted Fe-free and Fe-rich allophane revealed structural changes, including the formation of layered phyllosilicate-like structures within poorly crystalline agglomerates, after only a few months of reaction time. Such structural changes may be a useful tool for interpreting the weathering history of returned martian samples that have had limited interactions with liquid water.

Examination of Fe-free allophane, Fe-poor allophane, and Fe-rich allophane may be critical to understanding the

characteristics of short-lived martian waters. These phases may provide insight into the duration of short-lived liquid water in Gale crater by allowing examination of aqueous alteration features at a finer timescale than that provided by well crystalline, aqueously altered minerals. With continued investigation and characterization, the properties of the Mars amorphous component could be used to constrain and elucidate the characteristics of the most recent waters on Mars.

## ACKNOWLEDGMENTS

The authors acknowledge the following people for their contributions to this research: Brad Sutter, Lisa Danielson, Joanna Hogancamp, Toluwalope Bamisile, Chris Adcock, Seth Gainey, Peter Sbraccia, Arlaine Sanchez, Ngoc Luu, Dave Hatchett, Minghua Ren, Michael Strange, and Richard Panduro-Allanson. They also thank Editor-in-Chief Professor Joseph W. Stucki, the associate editors of *Clays and Clay Minerals*, and journal reviewers for their insightful comments on this manuscript. This work was supported by the NASA Mars Data Analysis Program (grant #80NSSC17K0581), the University of Nevada, Las Vegas Faculty Opportunity Award, the University of Nevada, Las Vegas Doctoral Award, the Geological Society of America Graduate Research Grant, the University of Nevada, Las Vegas Graduate and Professional Student Association research and travel grants, and the Southwest Travel Award.

## Funding

See Acknowledgments Section.

## Declarations

## Conflict of Interest

S. J. Ralston conducted this research while employed as a graduate student at the University of Nevada, Las Vegas and was employed by Jacobs ([www.jacobs.com](http://www.jacobs.com)) prior to manuscript submission (multiple affiliation). Elisabeth Hausrath, Oliver Tschauener, Elizabeth Rampe, Tanya Peretyazhko, Roy Christoffersen, Christopher DeFelice, and Hyejeong Lee declare that they have no conflicts to report.

## REFERENCES

- Abidin, Z., Matsue, N., & Henmi, T. (2004). Dissolution mechanism of nano-ball allophane with dilute alkali solution. *Clay Science*, *12*, 213–222.
- Achilles, C. N., Downs, R. T., Ming, D. W., Rampe, E. B., Morris, R. V., Treiman, A. H., Morrison, S. M., Blake, D. F., Vaniman, D. T., Ewing, R. C., Chipera, S. J., Yen, A. S., Bristow, T. F., Ehlmann, B. L., Gellert, R., Hazen, R. M., Fendrich, K. V., Craig, P. I., Grotzinger, J. P., ... Morookian, J. M. (2017). Mineralogy of an active eolian sediment from the Namib dune, Gale crater, Mars. *Journal of Geophysical Research, Planets*, *122*, 2344–2361.
- Baker, L. L., & Strawn, D. G. (2012). Fe K-edge XAFS spectra of phyllosilicates of varying crystallinity. *Physics and Chemistry of Minerals*, *39*, 675–684.
- Baker, L. L., & Strawn, D. G. (2014). Temperature effects on synthetic nontronite crystallinity and implications for nontronite formation in Columbia River Basalts. *Clays and Clay Minerals*, *62*, 89–101.
- Baker, L. L., Nickerson, R. D., & Strawn, D. G. (2014). XAFS study of Fe-substituted allophane and imogolite. *Clays and Clay Minerals*, *62*, 20–34.
- Baldermann, A., Dohrmann, R., Kaufhold, S., Nickel, C., Letofsky-Papst, I., & Dietzel, M. (2014). The Fe-Mg-saponite solid solution series—a hydrothermal synthesis study. *Clay Minerals*, *49*, 391–415.
- Beard, A. D., Downes, H., & Chaussidon, M. (2015). Petrology of a nonindigenous microgranitic clast in polymict ureilite EET 87720: Evidence for formation of evolved melt on an unknown parent body. *Meteoritics & Planetary Science*, *50*, 1613–1623.
- Bibring, J. P., Langevin, Y., Mustard, J. F., Poulet, F., Arvidson, R., Gendrin, A., Gondet, B., Mangold, N., Pinet, P., Forget, F., Berthe, M., Bibring, J. P., Gendrin, A., Gomez, C., Gondet, B., Jouget, D., Poulet, F., Soufflot, A., Vincendon, M., ... Neukum, G. (2006). Global mineralogical and aqueous mars history derived from OMEGA/Mars Express data. *Science*, *312*, 400–404.
- Bish, D. L., & Duffy, C. J. (1990). Thermogravimetric analysis of minerals. In *Thermal Analysis in Clay Science* (J. W. Stucki and D. L. Bish, Eds.), The Clay Minerals Society, Chantilly, VA, USA, (pp. 95–189).
- Bish, D.L., Blake, D.F., Vaniman, D.T., Chipera, S.J., Morris, R.V., Ming, D.W., Treiman, A.H., Sarrazin, P., Morrison, S.M., Downs, R.T., Achilles, C.N., Yen, A.S., Bristow, T.F., Crisp, J.A., Morookian, J.M., Farmer, J.D., Rampe, E.B., Stolper, E.M., Spanovich, N., & the MSL Science Team. (2013). X-ray diffraction results from Mars Science Laboratory: mineralogy of Rocknest at Gale crater. *Science*, *341*, 1238932.
- Bishop, J. L., & Rampe, E. B. (2016). Evidence for a changing Martian climate from the mineralogy at Mawrth Vallis. *Earth and Planetary Science, Letters*, *448*, 42–48.
- Bishop, J. L., Rampe, E. B., Bish, D. L., Abidin, Z., Baker, L. L., Matsue, N., & Henmi, T. (2013). Spectral and hydration properties of allophane and imogolite. *Clays and Clay Minerals*, *61*, 57–74.
- Blake, D.F., Morris, R.V., Kocurek, G., Morrison, S.M., Downs, R.T., Bish, D., Ming, D.W., Edgett, K.S., Rubin, D., Goetz, W., Madsen, M.B., Sullivan, R., Gellert, R., Campbell, I., Treiman, A.H., McLennan, S.M., Yen, A.S., Grotzinger, J., Vaniman, D.T., Chipera, S.J., Achilles, C.N., Rampe, E.B. Sumner, D., Meslin, P.Y., Maurice, S., Forni, O., Gasnault, O., Fisk, M., Schmidt, M., Mahaffy, P., Leshin, L.A., Glavin, D., Steele, A., Freissinet, C., Navarro-Gonzalez, R., Yingst, R.A., Kah, L.C., Bridges, N., Lewis, K.W., Bristow, T.F., Farmer, J.D., Crisp, J.A., Stolper, E.M., Marais, D.J.D., Sarrazin, P., & the MSL Science Team. (2013). Curiosity at Gale crater, Mars: Characterization and analysis of the Rocknest sand shadow. *Science*, *341*, 1239505.
- Bleeker, P., & Parfitt, R. L. (1974). Volcanic ash and its clay mineralogy at Cape Hoskins, New Britain, Papua New Guinea. *Geoderma*, *11*, 123–135.
- Carr, M. H. (1996). Water erosion on Mars and its biologic implications. *Endeavour*, *20*, 56–60.
- Catalano, J. G. (2013). Thermodynamic and mass balance constraints on iron-bearing phyllosilicate formation and

- alteration pathways on early Mars. *Journal of Geophysical Research, Planets*, 118, 2124–2136.
- Cheah, S.-F., Kraemer, S. M., Cervini-Silva, J., & Sposito, G. (2003). Steady-state dissolution kinetics of goethite in the presence of desferrioxamine B and oxalate ligands: implications for the microbial acquisition of iron. *Chemical Geology*, 198, 63–75.
- Childs, C. W., Parfitt, R. L., & Newman, R. H. (1990). Structural studies of Silica Springs allophane. *Clay Minerals*, 25, 329–341.
- Decarreau, A., Bonnin, D., Badaut-Trauth, D., Couty, R., & Kaiser, P. (1987). Synthesis and crystallogeneses of ferric smectite by evolution of Si-Fe coprecipitates in oxidizing conditions. *Clay Minerals*, 22, 207–223.
- DeFelice, C., Mallick, S., Saal, A. E., & Huang, S. (2019). An isotopically depleted lower mantle component is intrinsic to the Hawaiian mantle plume. *Nature Geoscience*, 12, 487–492.
- Dehouck, E., McLennan, S. M., Meslin, P. Y., & Cousin, A. (2014). Constraints on abundance, composition, and nature of X-ray amorphous components of soils and rocks at Gale crater, Mars. *Journal of Geophysical Research, Planets*, 119, 2640–2657.
- Dehouck, E., McLennan, S. M., Sklute, E. C., & Darby Dyar, M. (2017). Stability and fate of ferrihydrite during episodes of water/rock interactions on early Mars: An experimental approach. *Journal of Geophysical Research, Planets*, 122, 358–382.
- Denaix, L. (1993). Synthèse et propriétés d'aluminosilicates non lamellaires: l'imogolite et les allophanes, *Sciences de la Terre*. Université Pierre et Marie Curie (Paris 6), Paris, FRA, p. 223.
- Dove, P. M., & Crerar, D. A. (1990). Kinetics of quartz dissolution in electrolyte solutions using a hydrothermal mixed flow reactor. *Geochimica et Cosmochimica Acta*, 54, 955–969.
- Dove, P. M., & Nix, C. J. (1997). The influence of the alkaline earth cations, magnesium, calcium, and barium on the dissolution kinetics of quartz. *Geochimica et Cosmochimica Acta*, 61, 3329–3340.
- Eaton, A. D., Clesceri, L. S., Rice, E. W., Greenberg, A. E., & Franson, M. A. H. (2005). *Standard methods for the examination of water and wastewater*. American Public Health Association.
- Eggleton, R. A., & Tilley, D. B. (1998). Hisingerite: a ferric kaolin mineral with curved morphology. *Clays and Clay Minerals*, 46, 400–413.
- Elwood-Madden, M. E., Madden, A. S., & Rimstidt, J. D. (2009). How long was Meridiani Planum wet? Applying a jarosite stopwatch to determine the duration of aqueous diagenesis. *Geology*, 37, 635–638.
- Elwood-Madden, M. E., Madden, A. S., Rimstidt, J. D., Zahrai, S., Kendall, M. R., & Miller, M. A. (2012). Jarosite dissolution rates and nanoscale mineralogy. *Geochimica et Cosmochimica Acta*, 91, 306–321.
- Farmer, V. (1997). Conversion of ferruginous allophanes to ferruginous beidellites at 95°C under alkaline conditions with alternating oxidation and reduction. *Clays and Clay Minerals*, 45, 591–597.
- Farmer, V., Krishnamurti, G., & Huang, P. (1991). Synthetic allophane and layer-silicate formation in SiO<sub>2</sub>-Al<sub>2</sub>O<sub>3</sub>-FeO-Fe<sub>2</sub>O<sub>3</sub>-MgO-H<sub>2</sub>O systems at 23°C and 89°C in a calcareous environment. *Clays and Clay Minerals*, 39, 561–570.
- Frink, C. R., & Peech, M. (1963). Hydrolysis of the aluminum ion in dilute aqueous solutions. *Inorganic Chemistry*, 2, 473–478.
- Frushour, A.M. & Bish, D.L. (2017). Laboratory studies of smectite chloritization: applications to the clay mineralogy of Gale crater, Mars. *Lunar Planetary Science XLVIII*. Lunar Planetary Institute, Houston, #2622(abstr.).
- Frydenvang, J., Gasada, P. J., Hurowitz, J. A., Grotzinger, J. P., Wiens, R. C., Newsom, H. E., Edgett, K. S., Watkins, J., Bridges, J. C., Maurice, S., Risk, M. R., Johnson, J. R., Rapin, W., Stein, N. T., Clegg, S. M., Schwenzer, S. P., Bedford, C. C., Edwards, P., Mangold, N., ... Vasavada, A. R. (2017). Diagenetic silica enrichment and late-stage groundwater activity in Gale crater, Mars. *Geophysical Research Letters*, 44, 4716–4724.
- Gainey, S. R., Hausrath, E. M., Hurowitz, J. A., & Milliken, R. E. (2014). Nontronite dissolution rates and implications for Mars. *Geochimica et Cosmochimica Acta*, 126, 192–211.
- Gainey, S. R., Hausrath, E. M., Adcock, C. T., Tschauer, O., Hurowitz, J. A., Ehlmann, B. L., Xiao, Y., & Bartlett, C. L. (2017). Clay mineral formation under oxidized conditions and implications for paleoenvironments and organic preservation on Mars. *Nature Communications*, 8, 1230.
- Gautier, J.-M., Oelkers, E. H., & Schott, J. (2001). Are quartz dissolution rates proportional to B.E.T. surface areas? *Geochimica et Cosmochimica Acta*, 65, 1059–1070.
- Gibbons, R. D., Grams, N. E., Jarke, F. H., & Stoub, K. P. (1991). Practical quantitation limits. *Chemometrics and Intelligent Laboratory Systems*, 12, 225–235.
- Gislason, S. R., & Oelkers, E. H. (2003). Mechanism, rates, and consequences of basaltic glass dissolution: II. An experimental study of the dissolution rates of basaltic glass as a function of pH and temperature. *Geochimica et Cosmochimica Acta*, 67, 3817–3832.
- Goodyear, J., & Duffin, W. J. (1961). An X-ray examination of an exceptionally well crystallized kaolinite. *Mineralogical Magazine*, 32, 902–907.
- Grotzinger, J.P., Gupta, S., Malin, M.C., Rubin, D.M., Schieber, J., Siebach, K., Sumner, D.Y., Stack, K.M., Vasavada, A.R., Arvidson, R.E., Calef 3rd, F., Edgar, L., Fischer, W.F., Grant, J.A., Griffes, J., Kah, L.C., Lamb, M.P., Lewis, K.W., Mangold, N., Minitti, M.E., Palucis, M., Rice, M., Williams, R.M., Yingst, R.A., Blake, D., Blaney, D., Conrad, P., Crisp, J., Dietrich, W.E., Dromart, G., Edgett, K.S., Ewing, R.C., Gellert, R., Hurowitz, J.A., Kocurek, G., Mahaffy, P., McBride, M.J., McLennan, S.M., Mischna, M., Ming, D., Milliken, R., Newsom, H., Oehler, D., Parker, T.J., Vaniman, D., Wiens, R.C., & Wilson, S.A. (2015). Deposition, exhumation, and paleoclimate of an ancient lake deposit, Gale crater, Mars. *Science*, 350, aac7575.
- Gustafsson, J.P., Karlton, E., & Bhattacharya P. (1998). *Allophane and imogolite in Swedish soils*. Royal Institute of Technology (KTH), Stockholm.
- Harder, H. (1976). Nontronite synthesis at low temperatures. *Chemical Geology*, 18, 169–180.
- Harder, H. (1978). Synthesis of iron layer silicate minerals under natural conditions. *Clays and Clay Minerals*, 26, 65–72.

- Hausrath, E. M., Ming, D. W., Peretyazhko, T. S., & Rampe, E. B. (2018). Reactive transport and mass balance modeling of the Stimson sedimentary formation and altered fracture zones constrain diagenetic conditions at Gale crater, Mars. *Earth and Planetary Science Letters*, *491*, 1–10.
- Helm, L., & Merbach, A. E. (2005). Inorganic and bioinorganic solvent exchange mechanisms. *Chemical Reviews*, *105*, 1923–1959.
- Henmi, T., Wells, N., Childs, C. W., & Parfitt, R. L. (1980). Poorly-ordered iron-rich precipitates from springs and streams on andesitic volcanoes. *Geochimica et Cosmochimica Acta*, *44*, 365–372.
- Hisinger, W. (1828). Analyse des mit dem Namen Hisingerit belegten Eisensilicats. *Annalen der Physik und Chemie von J.C. Poggendorff Bd*, *13*, 13–508.
- Hsu, P. H. (1976). Comparison of iron(III) and aluminum in precipitation of phosphate from solution. *Water Research*, *10*, 903–907.
- Huertas, F. J., Caballero, E., Jiménez de Cisneros, C., Huertas, F., & Linares, J. (2001). Kinetics of montmorillonite dissolution in granitic solutions. *Applied Geochemistry*, *16*, 397–407.
- Huffman, E.O. (1960). Rates and mechanisms of dissolution of some ferric phosphates. *Soil Science*, 1–8.
- Icenhower, J. P., & Dove, P. M. (2000). The dissolution kinetics of amorphous silica into sodium chloride solutions: Effects of temperature and ionic strength. *Geochimica et Cosmochimica Acta*, *64*, 4193–4203.
- Ingles, O. G., & Willoughby, D. R. (1967). An occurrence of hisingerite with evidence of its genesis. *Soil Science*, *104*, 383–385.
- Iyoda, F., Hayashi, S., Arakawa, S., John, B., Okamoto, M., Hayashi, H., & Yuan, G. D. (2012). Synthesis and adsorption characteristics of hollow spherical allophane nano-particles. *Applied Clay Science*, *56*, 77–83.
- Jeute, T., Baker, L. L., Bishop, J. L., Abidin, Z., & Rampe, E. B. (2021). Spectroscopic analysis of allophane and imogolite samples with variable Fe abundance for characterizing the poorly crystalline components on Mars. *American Mineralogist*, *106*, 527–540.
- Karube, J., Nakaishi, K., Sugimoto, H., & Fujihira, M. (1996). Size and shape of allophane particles in dispersed aqueous systems. *Clays and Clay Minerals*, *44*, 485–491.
- Kitagawa, Y. (1973). Substitution of aluminum in allophane by iron. *Clay Science*, *4*, 151–154.
- Kitagawa, Y. (1974). Dehydration of allophane and its structural formula. *American Mineralogist*, *59*, 1094–1098.
- Klopprogge, J. T., Evans, R., Hickey, L., & Frost, R. L. (2002). Characterization and Al-pillaring of smectites from Miles, Queensland (Australia). *Applied Clay Science*, *20*, 157–163.
- Lamb, A. B., & Jacques, A. G. (1938). The slow hydrolysis of ferric chloride in dilute solutions—II. The change in hydrogen ion concentration. *Journal of the American Chemical Society*, *60*, 1215–1225.
- Lasaga, A. C. (1984). Chemical kinetics of water–rock interactions. *Journal of Geophysical Research*, *89*, 4009–4025.
- Leshin, L.A., Mahaffy, P.R., Webster, C.R., Cabane, M., Coll, P., Conrad, P.G., Archer Jr., P.D., Atreya, S.K., Brunner, A.E., Buch, A., Eigenbrode, J.L., Flesch, G.J., Franz, H.B., Freissinet, C., Glavin, D.P., McAdam, A.C., Miller, K.E., Ming, D.W., Morris, R.V., Navarro-Gonzalez, R., Niles, P.B., Owen, T., Pepin, R.O., Squyres, S., Steele, A., Stern, J.C., Summons, R.E., Sumner, D.Y., Sutter, B., Szopa, C., Teinturier, S., Trainer, M.G., Wray, J.J., Grotzinger, J.P., & the MSL Science Team. (2013). Volatile, isotope, and organic analysis of martian fines with the Mars Curiosity rover. *Science*, *341*, 1238937.
- Liang, D.-T., & Readey, D. W. (1987). Dissolution kinetics of crystalline and amorphous silica in hydrofluoric-hydrochloric acid mixtures. *Journal of the American Ceramic Society*, *70*, 570–577.
- Meslin, P.Y., Gasnault, O., Forni, O., Schroder, S., Cousin, A., Berger, G., Clegg, S.M., Lasue, J., Maurice, S., Sautter, V., Le Mouelic, S., Wiens, R.C., Fabre, C., Goetz, W., Bish, D., Mangold, N., Ehlmann, B., Lanza, N., Harri, A.M., Anderson, R., Rampe, E., McConnochie, T.H., Pinet, P., Blaney, D., Leveille, R., Archer, D., Barraclough, B., Bender, S., Blake, D., Blank, J.G., Bridges, N., Clark, B.C., DeFlores, L., Delapp, D., Dromart, G., Dyar, M.D., Fisk, M., Gondet, B., Grotzinger, J., Herkenhoff, K., Johnson, J., Lacour, J.L., Langevin, Y., Leshin, L., Lewin, E., Madsen, M.B., Melikechi, N., Mezzacappa, A., Mischna, M.A., Moores, J.E., Newsom, H., Ollila, A., Perez, R., Renno, N., Sirven, J.B., Tokar, R., de la Torre, M., d'Uston, L., Vaniman, D., Yingst, A., & the MSL Science Team (2013). Soil diversity and hydration as observed by ChemCam at Gale crater, Mars. *Science*, *341*.
- Miller, J. L., Elwood-Madden, A. S., Phillips-Lander, C. M., Pritchett, B. N., & Elwood-Madden, M. E. (2016). Alunite dissolution rates: Dissolution mechanisms and implications for Mars. *Geochimica et Cosmochimica Acta*, *172*, 93–106.
- Milliken, R.E. & Bish D.L. (2014). Distinguishing hisingerite from other clays and its importance for Mars. *Lunar and Planetary Science XLV*. Lunar Planetary Institute, Houston, #2251(abstr.).
- Milliken, R. E., Swayze, G. A., Arvidson, R. E., Bishop, J. L., Clark, R. N., Ehlmann, B. L., Green, R. O., Grotzinger, J. P., Morris, R. V., Murchie, S. L., Mustard, J. F., & Weitz, C. (2008). Opaline silica in young deposits on Mars. *Geology*, *36*, 847.
- Montarges-Pelletier, E., Bogenez, S., Pelletier, M., Razafitianamaharavo, A., Ghanbaja, J., Lartiges, B., & Michot, L. (2005). Synthetic allophane-like particles: textural properties. *Colloids and Colloid Surfaces A: Physicochemical and Engineering Aspects*, *255*, 1–10.
- Moore, D. M., & Reynolds, R. C. (1997). *X-ray Diffraction and the Identification and Analysis of Clay Minerals*. (2nd ed., p. 378). Oxford University Press, New York.
- Morris, R. V., Golden, D. C., Bell, J. F., Shelfer, T. D., Scheinost, A. C., Hinman, N. W., Furniss, G., Mertzman, S. A., Bishop, J. L., Ming, D. W., Allen, C. C., & Britt, D. T. (2000). Mineralogy, composition, and alteration of Mars Pathfinder rocks and soils: Evidence from multispectral, elemental, and magnetic data on terrestrial analogue, SNC meteorite, and Pathfinder samples. *Journal of Geophysical Research, Planets*, *105*, 1757–1817.
- Morris, R. V., Vaniman, D. T., Blake, D. F., Gellert, R., Chipera, S. J., Rampe, E. B., Ming, D. W., Morrison, S. M., Downs, R. T., Treiman, A. H., Yen, A. S., Grotzinger, J. P., Achilles, C. N., Bristow, T. F., Crisp, J. A., Des Marais, D. J., Farmer, J. D., Fendrich, K. V., Frydenvang, J., ... Schwenzer, S. P. (2016). Silicic volcanism on Mars evidenced by tridymite in high-SiO<sub>2</sub> sedimentary rock at Gale crater. *Proceedings of the National*



- Academy of Sciences of the United States of America, 113, 7071–7076.
- Morrison, S. M., Downs, R. T., Blake, D. F., Vaniman, D. T., Ming, D. W., Hazen, R. M., Treiman, A. H., Achilles, C. N., Yen, A. S., Morris, R. V., Rampe, E. B., Bristow, T. F., Chipera, S. J., Sarrazin, P. C., Gellert, R., Fendrich, K. V., Morookian, J. M., Farmer, J. D., Des Marais, D. J., & Craig, P. I. (2018). Crystal chemistry of martian minerals from Bradbury Landing through Naukluft Plateau, Gale crater, Mars. *American Mineralogist*, 103, 857–871.
- Mustoe, G. E. (1996). Hisingerite – A rare iron mineral from walker Valley, Skagit County, Washington. *Washington Geology*, 24, 14–19.
- Nagasawa, K. (1978). Weathering of volcanic ash and other pyroclastic materials. Pp. 105–125 in: *Clays and Clay Minerals, of Japan* (T. Sudo and S. Shimoda, editors). Elsevier Science Publishing Company, Amsterdam.
- Nagy, K. L., Blum, A. E., & Lasaga, A. C. (1991). Dissolution and precipitation kinetics of kaolinite at 80°C and pH 3: the dependence on solution saturation state. *American Journal of Science*, 291, 649–696.
- Ohashi, F., Wada, S. I., Suzuki, M., Maeda, M., & Tomura, S. (2002). Synthetic allophane from high-concentration solutions: nanoengineering of the porous solid. *Clay Minerals*, 37, 451–456.
- Olsen, A. A., Hausrath, E. M., & Rimstidt, J. D. (2015). Forsterite dissolution rates in Mg-sulfate-rich Mars-analog brines and implications of the aqueous history of Mars. *Journal of Geophysical Research, Planets*, 120, 388–400.
- Ossaka, J., Iwai, S.-I., Kasai, M., Shirai, T., & Hamada, S. (1971). Coexistence states of iron in synthesized iron-bearing allophane (Al<sub>2</sub>O<sub>3</sub>-SiO<sub>2</sub>-Fe<sub>2</sub>O<sub>3</sub>-H<sub>2</sub>O system). *Bulletin of the Chemical Society of Japan*, 44, 716–718.
- Palandri, J.L. & Kharaka, Y.K. (2004). A compilation of rate parameters of water-mineral interaction kinetics for application to geochemical modeling. U.S. Geological Survey Water-Resources Investigations Report 04–1068.
- Parfitt, R. L. (1990). Allophane in New Zealand – a review. *Australian Journal of Soil Research*, 28, 343–360.
- Parfitt, R. L. (2009). Allophane and imogolite: role in soil biogeochemical processes. *Clay Minerals*, 44, 135–155.
- Pickering, R. (2014). *Tri-Octahedral Domains and Crystallinity in Synthetic Clays: Implications for Lacustrine Paleoenvironmental Reconstruction*. Georgia State University.
- Potts, P. J., Webb, P. C., & Watson, J. S. (1984). Energy dispersive X-ray fluorescence analysis of silicate rocks for major and trace elements. *X-Ray Spectrometry*, 13, 2–15.
- Pritchett, B. N., Madden, M.E.E., & Madden, A.S. (2012). Jarosite dissolution rates and maximum lifetimes in high salinity brines: Implications for Earth and Mars. *Earth and Planetary Science Letters*, 357, 327–336.
- Rampe, E.B., Kraft, M.D., Sharp, T.G., Golden, D.C., Ming, D.W., Christensen, P.R., & Ruff S.W. (2011). Detection of allophane on Mars through orbital and in situ thermal infrared spectroscopy. *Lunar and Planetary Science XLII*. Lunar and Planetary Institute, Houston, #2145(abstract).
- Rampe, E. B., Kraft, M. D., Sharp, T. G., Golden, D. C., Ming, D. W., & Christensen, P. R. (2012). Allophane detection on Mars with Thermal Emission Spectrometer data and implications for regional-scale chemical weathering processes. *Geology*, 40, 995–998.
- Rampe, E. B., Morris, R. V., Archer, P. D., Agresti, D. G., & Ming, D. W. (2016). Recognizing sulfate and phosphate complexes chemisorbed onto nanophase weathering products on Mars using in situ and remote observations. *American Mineralogist*, 101, 678–689.
- Rampe, E. B., Ming, D. W., Blake, D. F., Bristow, T. F., Chipera, S. J., Grotzinger, J. P., Morris, R. V., Morrison, S. M., Vaniman, D. T., Yen, A. S., Achilles, C. N., Craig, P. I., Des Marais, D. J., Downs, R. T., Farmer, J. D., Fendrich, K. V., Gellert, R., Hazen, R. M., Kah, L. C., ... Thompson, L. M. (2017). Mineralogy of an ancient lacustrine mudstone succession from the Murray formation, Gale crater, Mars. *Earth and Planetary Science Letters*, 471, 172–185.
- Rampe, E. B., Lapotre, M. G. A., Bristow, T. F., Arvidson, R. E., Morris, R. V., Achilles, C. N., Weitz, C., Blake, D. F., Ming, D. W., Morrison, S. M., Vaniman, D. T., Chipera, S. J., Downs, R. T., Grotzinger, J. P., Hazen, R. M., Peretyazhko, T. S., Sutter, B., Tu, V., Yen, A. S., ... Treiman, A. H. (2018). Sand mineralogy within the Bag-nold Dunes, Gale Crater, as Observed in situ and from orbit. *Geophysical Research Letters*, 45, 9488–9497.
- Rampe, E. B., Blake, D.F., Bristow, T.F., Ming, D.W., Vaniman, D.T., Morris, R.V., Achilles, C.N., Chipera, S.J., Morrison, S.M., Tu, V.M., Yen, A.S., Castle, N., Downs, G.W., Downs, R.T., Grotzinger, J.P., Hazen, R.M., Treiman, A.H., Peretyazhko, T.S., Des Marais, D.J., Walroth, R.C., Craig, P.I., Crisp, J.A., Lafuente, B., Morookian, J.M., Sarrazin, P.C., Thorpe, M.T., Bridges, J.C., Edgar, L.A., Fedo, C.M., Freissinet, C., Gellert, R., Mahaffy, P.R., Newsom, H.E., Johnson, J.R., Kah, L.C., Siebach, K.L., Schieber, J., Sun, V.Z., Vasavada, A.R., Wellington, D., Wiens, R.C., and the MSL Science Team. (2020). Mineralogy and geochemistry of sedimentary rocks and eolian sediments in Gale crater, Mars: A review after six Earth years of exploration with Curiosity. *Geochemistry*, 80, 125605.
- Rimstidt, J. D., & Barnes, H. L. (1980). The kinetics of silica-water reactions. *Geochimica et Cosmochimica Acta*, 44, 1683–1700.
- Rozalen, M. L., Huertas, F. J., Brady, P. V., Cama, J., García-Palma, S., & Linares, J. (2008). Experimental study of the effect of pH on the kinetics of montmorillonite dissolution at 25°C. *Geochimica et Cosmochimica Acta*, 72, 4224–4253.
- Sanders, R. L., Washton, N. M., & Mueller, K. T. (2012). Atomic-level studies of the depletion in reactive sites during clay mineral dissolution. *Geochimica et Cosmochimica Acta*, 92, 100–116.
- Shayan, A. (1984). Hisingerite material from a basalt quarry near Geelong, Victoria, Australia. *Clays and Clay Minerals*, 32, 272–278.
- Shayan, A., Sanders, J. V., & Lancucki, C. J. (1988). Hydrothermal alterations of hisingerite material from a basalt quarry near Geelong, Victoria, Australia. *Clays and Clay Minerals*, 36, 327–336.
- Singer, R. B. (1985). Spectroscopic observation of Mars. *Advances in Space Research*, 5, 59–68.
- Smith, R. J., Rampe, E. B., Horgan, B. H. N., & Dehouck, E. (2018). Deriving amorphous component abundance and composition of rocks and sediments on Earth and Mars. *Journal of Geophysical Research, Planets*, 123, 2485–2505.

- Squyres, S. W., Arvidson, R. E., Ruff, S., Gellert, R., Morris, R. V., Ming, D. W., Crumpler, L., Farmer, J. D., Des Marais, D. J., Yen, A., McLennan, S. M., Calvin, W., Bell, J. F., 3rd., Clark, B. C., Wang, A., McCoy, T. J., Schmidt, M. E., & de Souza Jr., P. A. (2008). Detection of silica-rich deposits on Mars. *Science*, *320*, 1063–1067.
- Steiner, M. H., Hausrath, E. M., Elwood-Madden, M. E., Tschauner, O., Ehlmann, B. L., Olsen, A. A., Gainey, S. R., & Smith, J. S. (2016). Dissolution of nontronite in chloride brines and implications for the aqueous history of Mars. *Geochimica et Cosmochimica Acta*, *195*, 259–276.
- Stillings, L. L., & Brantley, S. L. (1995). Feldspar dissolution at 25°C and pH 3: reaction stoichiometry and the effect of cations. *Geochimica et Cosmochimica Acta*, *59*, 1483–1496.
- Sun, Z., Zhou, H., Glasby, G., Yang, Q., Yin, X., Li, J., & Chen, Z. (2011). Formation of Fe-Mn-Si oxide and nontronite deposits in hydrothermal fields on the Valu Fa Ridge, Lau Basin. *Journal of Asian Earth Sciences*, *43*, 64–76.
- Sutter, B., McAdam, A. C., Mahaffy, P. R., Ming, D. W., Edgett, K. S., Rampe, E. B., Eigenbrode, J. L., Franz, H. B., Freissinet, C., Grotzinger, J. P., Steele, A., House, C. H., Archer, P. D., Malespin, C. A., Navarro-González, R., Stern, J. C., Bell, J. F., Calef, F. J., Gellert, R., ... Yen, A. S. (2017). Evolved gas analyses of sedimentary rocks and eolian sediment in Gale crater, Mars: Results of the Curiosity rover's sample analysis at Mars instrument from Yellowknife Bay to the Namib Dune. *Journal of Geophysical Research, Planets*, *122*, 2574–2609.
- Theng, B. K. G., Russell, M., Churchman, G. J., & Parfitt, R. L. (1982). Surface properties of allophane, halloysite, and imogolite. *Clays and Clay Minerals*, *30*, 143–149.
- Tosca, N. J., Knoll, A. H., & McLennan, S. M. (2008). Water activity and the challenge for life on early Mars. *Science*, *320*, 1204–1207.
- Treiman, A. H., Bish, D. L., Vaniman, D. T., Chipera, S. J., Blake, D. F., Ming, D. W., Morris, R. V., Bristow, T. F., Morrison, S. M., Baker, M. B., Rampe, E. B., Downs, R. T., Filiberto, J., Glazner, A. F., Gellert, R., Thompson, L. M., Schmidt, M. E., Le Deit, L., Wiens, R. C., ... Yen, A. S. (2016). Mineralogy, provenance, and diagenesis of a potassic basaltic sandstone on Mars: CheMin X-ray diffraction of the Windjana sample (Kimberley area, Gale Crater). *Journal of Geophysical Research, Planets*, *121*, 75–106.
- Tu, V. M., Hausrath, E. M., Tschauner, O., Iota, V., & Egeland, G. W. (2014). Dissolution rates of amorphous Al- and Fe-phosphates and their relevance to phosphate mobility on Mars. *American Mineralogist*, *99*, 1206–1215.
- Van der Gaast, S. J., & Vaars, A. J. (1981). A method to eliminate the background in X-ray-diffraction patterns of oriented clay mineral samples. *Clay Minerals*, *16*, 383–393.
- Vaniman, D. T., Bish, D. L., Ming, D. W., Bristow, T. F., Morris, R. V., Blake, D. F., Chipera, S. J., Morrison, S. M., Treiman, A. H., Rampe, E. B., Rice, M., Achilles, C. N., Grotzinger, J. P., McLennan, S. M., Williams, J., Bell 3rd, J. F., Newsom, H. E., Downs, R. T., Maurice, S., Sarrazin, P., Yen, A. S., Morookian, J. M., Farmer, J. D., Stack, K., Milliken, R. E., Ehlmann, B. L., Sumner, D. Y., Berger, G., Crisp, J. A., Hurowitz, J. A., Anderson, R., Des Marais, D. J., Stolper, E. M., Edgett, K. S., Gupta, S., Spanovich, N., & the MSL Science Team. (2014). Mineralogy of a mudstone at Yellowknife Bay, Gale crater, Mars. *Science*, *343*, 1243480.
- Vaniman, D. T., Martínez, G. M., Rampe, E. B., Bristow, T. F., Blake, D. F., Yen, A. S., Ming, D. W., Rapin, W., Meslin, P.-Y., Morookian, J. M., Downs, R. T., Chipera, S. J., Morris, R. V., Morrison, S. M., Treiman, A. H., Achilles, C. N., Robertson, K., Grotzinger, J. P., Hazen R. M., Wiens, R. C., & Sumner, D. Y. (2018). Gypsum, bassanite, and anhydrite at Gale crater, Mars. *American Mineralogist*, *103*, 1011–1020.
- Velbel, M. A. (1993). Constancy of silicate-mineral weathering-rate ratios between natural and experimental weathering: implications for hydrologic control of differences in absolute rates. *Chemical Geology*, *105*, 89–99.
- Wada, K. (1989). Allophane and imogolite. In: *Minerals in Soil Environments* (J. B. Dixon and S. B. Weed, (Eds.), Soil Science Society of America, Madison, WI, USA. (pp. 1051–1087).
- Wada, K., & Yoshinaga, N. (1969). The structure of imogolite. *American Mineralogist*, *54*, 50–71.
- Weitz, C. M., Bishop, J. L., Baker, L. L., & Berman, D. C. (2014). Fresh exposures of hydrous Fe-bearing amorphous silicates on Mars. *Geophysical Research Letters*, *41*, 8744–8751.
- Welch, S. A., & Ullman, W. J. (2000). The temperature dependence of bytownite feldspar dissolution in neutral aqueous solutions of inorganic and organic ligands at low temperature (5–35°C). *Chemical Geology*, *167*, 337–354.
- Wogelius, R. A., & Walther, J. V. (1991). Olivine dissolution at 25°C: effects of pH, CO<sub>2</sub>, and organic acids. *Geochimica et Cosmochimica Acta*, *55*, 943–954.
- Yen, A. S., Ming, D. W., Vaniman, D. T., Gellert, R., Blake, D. F., Morris, R. V., Morrison, S. M., Bristow, T. F., Chipera, S. J., Edgett, K. S., Treiman, A. H., Clark, B. C., Downs, R. T., Farmer, J. D., Grotzinger, J. P., Rampe, E. B., Schmidt, M. E., Sutter, B., & Thompson, L. M. (2017). Multiple stages of aqueous alteration along fractures in mudstone and sandstone strata in Gale crater, Mars. *Earth and Planetary Science Letters*, *471*, 186–198.
- Zhu, C., Liu, Z., Zhang, Y., Wang, C., Scheafer, A., Lu, P., Zhang, G., Georg, R. B., Yuan, H., & Rimstidt, J. D. (2016). Measuring silicate mineral dissolution rates using Si isotope dating. *Chemical Geology*, *445*, 146–163.

(Received 16 September 2020; revised 11 March 2021; AE: F. Javier Huertas)